

# Orbital moiré and quadrupolar triple- $q$ physics in a triangular lattice

Kazumasa Hattori\*

Department of Physics, Tokyo Metropolitan University,  
1-1, Minami-osawa, Hachioji, Tokyo 192-0397, Japan

Takayuki Ishitobi

Advanced Science Research Center, Japan Atomic Energy Agency, Tokai, Ibaraki 319-1195, Japan

Hirokazu Tsunetsugu

The Institute for Solid State Physics, The University of Tokyo, Kashiwanoha 5-1-5, Chiba 277-8581, Japan

(Dated: August 21, 2024)

We numerically study orders of planer type  $(xy, x^2 - y^2)$  quadrupoles on a triangular lattice with nearest-neighbor isotropic  $J$  and anisotropic  $K$  interactions. This type of quadrupoles possesses unique single-ion anisotropy proportional to a third order of the quadrupole moments. This provides an unconventional mechanism of triple- $q$  orders which does not exist for the degrees of freedom with odd parity under time-reversal operation such as magnetic dipoles. In addition to several single- $q$  orders, this system exhibits various orders including incommensurate triple- $q$  quasi-long-range orders and a four-sublattice triple- $q$  partial order. Our Monte-Carlo simulations demonstrate that the phase transition to the latter triple- $q$  state belongs to the universality class of the critical line of the Ashkin-Teller model in two dimensions close to the four-state Potts class. These results indicate a possibility of realizing this unique quadrupole textures in simple triangular systems.

*Introduction.*— Superposition of multiple standing waves creates a moiré texture, and this is recognized in our daily life, e.g., when looking at overlapped fences, lace curtains swaying in the wind, and known as notorious wavy patterns in photography and its post processing<sup>1</sup>. This visually fascinating texture is characterized by multiple wave vectors  $\{\mathbf{q}_\ell\}$ . Recent evolution of “moiré engineering” has been developed<sup>2,3</sup> for twisted graphene multilayers<sup>4-6</sup> and transition metal dichalcogenides<sup>7-9</sup> and this opens a novel way to manipulate their functionality and physics itself such as superconductivity<sup>4</sup>, nonreciprocal phenomena<sup>10</sup>, flat bands<sup>11</sup> and magnetoelectric effects<sup>12,13</sup>.

Another realization of moiré structure uses topological texture of internal degrees of freedom. Representative examples are superfluid He<sup>14</sup>, various types of superconductors<sup>15-17</sup>, Bose-Einstein condensates in cold atoms<sup>18-20</sup>, and exciton-polariton condensates<sup>21-23</sup>. This started in magnetic systems from the seminal work about quasi long-range orders in planer magnets<sup>24</sup> and this has opened a way toward topological physics. The discovery of skyrmion crystal in MnSi<sup>25-27</sup> triggered current explosion of researches which aim realizing moiré structure<sup>28</sup>. Such a spin moiré<sup>29,30</sup> is also realized by a crystallization of various topological defects<sup>31-33</sup>. Clarifying their properties is important for understanding the fundamental physics and also for developing the next generation technology.

Spatial modulations of a moiré structure are characterized by a set of ordering vectors  $\{\mathbf{q}_\ell\}$  ( $\ell = 1, 2, \dots$ ). This requires a multiple- $q$  order of order parameter, and control of the ordering vectors  $\{\mathbf{q}_\ell\}$  is an important issue. Ferromagnets with noncentrosymmetric structure have the Dzyaloshinskii-Moriya interaction<sup>34</sup> and it shifts the ordering vector  $\mathbf{q}$  from  $\mathbf{0}$  to finite incommensurate (IC) values. Such an IC ordering is also established by other mechanisms such as geometrical frustration<sup>35</sup>, Fermi-surface effects in itinerant electron systems<sup>36,37</sup>, and anisotropic interactions<sup>38-40</sup>. These varieties of possibility opens a wider range of material research

for realizing multiple- $q$  orders<sup>41</sup>.

Recently, several studies have tried realizing multiple- $q$  orders of nonmagnetic degrees of freedom  $\varphi$  such as electric charge<sup>42,43</sup> and electric quadrupole<sup>44-46</sup>. These order parameters are time-reversal even, which differs from magnetic ones. This makes a crude difference in their free energy from the magnetic counterpart<sup>43,47-50</sup>, and, for example, the cubic terms  $\varphi_\alpha \varphi_\beta \varphi_\gamma$  are allowed. Such terms may arise from a single-ion anisotropy and favor triple- $q$  orders, since the term  $\propto \varphi_\alpha(\mathbf{q}_1) \varphi_\beta(\mathbf{q}_2) \varphi_\gamma(\mathbf{q}_3) \delta_{\mathbf{q}_1 + \mathbf{q}_2 + \mathbf{q}_3, \mathbf{0}}$  lowers the free energy by properly choosing the phase and direction of each  $\varphi(\mathbf{q}_\ell)$ . Thus, nonmagnetic systems have a potential to exhibit multiple- $q$  physics, and provide a good playground for the moiré engineering.

In this Letter, we propose a minimal model and demonstrate that nonmagnetic systems are useful for realizing moiré textures. The model is defined for electric quadrupoles on a triangular lattice with nearest-neighbor interactions and we have performed Monte Carlo simulations for its effective classical Hamiltonian. In addition to varieties of phases, we have found IC triple- $q$  quasi long-range orders relevant to the two-dimensional Ashkin-Teller and Potts models with the partial ordering of quadrupole moments.

*Model.*—We consider a triangular lattice with the hexagonal site symmetry of the point group  $D_6$  or  $C_{6v}$ . In this case, the order parameter with the symmetry of  $\Gamma_5$  ( $E_2$ ) doublet is particularly interesting as will be explained below. This is the two-component quadrupole  $(\phi_u, \phi_v)$  with the symmetry of  $(2xy, x^2 - y^2)$ , and we ignore magnetic sectors, which might be present in real materials, for simplicity. We use a classical approximation to represent this quadrupole moment by a unit vector pointing to the direction denoted by  $\theta_r$ .

$$\phi_{\mathbf{r}} = (\phi_{u,\mathbf{r}}, \phi_{v,\mathbf{r}}) =: \hat{e}(\theta_r), \quad \hat{e}(\theta) \equiv (\cos \theta, \sin \theta), \quad (1)$$

where  $\mathbf{r}$  is the site position. We will use  $\hat{e}$  also for other vectors along with  $\hat{e}_\ell \equiv \hat{e}(\ell\omega)$  for the special angle  $\omega \equiv \frac{2\pi}{3}$ . These

two-component quadrupoles possess a local cubic coupling as a single-ion anisotropy:

$$V = \lambda \sum_{\mathbf{r}} (3\phi_{u,\mathbf{r}}^2 - \phi_{v,\mathbf{r}}^2) \phi_{v,\mathbf{r}} = \lambda \sum_{\mathbf{r}} \sin 3\theta_{\mathbf{r}}. \quad (2)$$

Without loss of generality we can set  $\lambda \geq 0$ .

Now let us introduce exchange couplings for the quadrupole moments. Each nearest-neighbor pair  $\phi_{\mathbf{r}}$  and  $\phi_{\mathbf{r}+\mathbf{d}}$  interact via two types of exchange couplings: an isotropic  $J$  and an anisotropic  $K$  one as

$$\mathcal{H}_{\text{ex}} = \sum_{\mathbf{r},\mathbf{d}} \sum_{ij} [(J-K)\delta_{ij} + 2Kd_id_j] \phi_{i,\mathbf{r}+\mathbf{d}} \phi_{j,\mathbf{r}}. \quad (3)$$

Here,  $\mathbf{r}$  runs over the sites on the triangular lattice.  $\mathbf{d}$  runs over a half of the nearest neighbors  $\mathbf{d} \equiv (d_u, d_v) \in \{\hat{e}_n\}_{n=0}^2$ . Then, the Hamiltonian is the sum of the two terms  $\mathcal{H} = \mathcal{H}_{\text{ex}} + V$ .

*Ordering vectors.*—Let us first examine the single- $\mathbf{q}$  spiral orders  $\phi_{\mathbf{r}} \propto \text{Re} \phi(\mathbf{q}^*) \exp(\pm i\mathbf{q}^* \cdot \mathbf{r})$ , and determine the value of ordering vector  $\mathbf{q}^*$ . See Appendix A. One can easily find that the order is ferroic ( $\mathbf{q}^* = \mathbf{0}$ ) when  $2J < -|K|$ . When  $-|K| < 2J < 5|K|$ , the order is commensurate antiferroic (AF) and  $\mathbf{q}^*$  locates at one of the edge centers (the M points) in the Brillouin zone (BZ):  $\mathbf{Q}_{\ell} = \frac{2\pi}{\sqrt{3}} \hat{e}((\frac{1}{4} - \ell)\omega)$  ( $\ell = 1, 2, 3$ ).

An interesting part is the IC state for the region of  $5|K| < 2J$ . As  $|K|$  decreases,  $\mathbf{q}^*$  leaves  $\mathbf{Q}_{\ell}$  and moves along the BZ edge:  $\mathbf{q}_{\ell}^* = \mathbf{Q}_{\ell} + \Delta_{\text{M}} \hat{e}_{4-\ell}$  with  $\cos(\Delta_{\text{M}}/2) = (2J + |K|)/(4J - 4|K|)$  and it reaches the BZ corner [K or K' point;  $\mathbf{q}_{\text{K}} = 2\omega \hat{e}_0$  and  $\mathbf{q}_{\text{K}'} = 2\omega \hat{e}(\frac{5}{2}\omega)$ ] when  $K = 0$ . As shown in Figs. 1(a) and (b), the lowest-energy eigenmodes  $\phi(\mathbf{q}_{\ell}^*)$  differ between distinct edges, but remain unchanged on each edge irrespective of  $\Delta_{\text{M}}$ :  $\phi(\mathbf{q}_{\ell}^*) \propto \mathbf{v}_{\ell}^+ = \hat{e}((\ell - \frac{1}{4})\omega)$  or  $\mathbf{v}_{\ell}^- = \hat{e}_{\ell-1}$ .

*Ferroic, AF 120°, and triple- $\mathbf{q}$  orders.*—Now that  $\mathbf{q}_{\ell}^*$ 's are determined, the classical solution of  $\phi_{\mathbf{r}}$  is readily obtained. However, the cubic potential (2) causes nontrivial modifications. Before their discussion, let us analyze simpler parts, *i.e.*, the ferroic (F) order for  $2J < -|K|$  and the 120° AF order for  $5|K| < 2J$ . See Fig. 1(c). Owing to the cubic term (2), these phases have no continuous degeneracy, and the moment's direction is locked at  $\theta_{\mathbf{r}} = (n_{\mathbf{r}} + \frac{3}{4})\omega$  with  $n_{\mathbf{r}} \in \{0, 1, 2\}$ .

For  $0 < 2J < 5K$ , the simplest candidate is the symmetric triple- $\mathbf{q}$  (sTQ) state. The three ordering vectors locate at  $\mathbf{Q}_{\ell}$ 's with an identical amplitude  $\phi_{\ell} \equiv |\phi(\mathbf{Q}_{\ell})|$  for all  $\ell$ . Note that  $\phi(\mathbf{Q}_{\ell})$ 's are all real since  $-\mathbf{Q}_{\ell} \equiv \mathbf{Q}_{\ell}$ . The  $\mathbf{v}_{\ell}^+$  mode has a lower energy of  $\mathcal{H}_{\text{ex}}$  than the  $\mathbf{v}_{\ell}^-$  mode's, and this comprises the triple- $\mathbf{q}$  configuration

$$\phi_{\mathbf{r}} = \sum_{\ell=1,2,3} \phi_{\ell} \cos(\mathbf{Q}_{\ell} \cdot \mathbf{r}) \sigma_{\ell} \mathbf{v}_{\ell}^+, \quad \sigma_{\ell} \in \{+1, -1\}. \quad (4)$$

Substituting this with  $\phi_{\ell} = \frac{1}{2}\phi > 0$  in Eq. (2), one finds  $V = -\frac{3}{4}N\lambda\phi^3\sigma_1\sigma_2\sigma_3$ , where  $N$  is the number of sites. This term is minimized when all three or otherwise one of  $\sigma_{\ell}$ 's is +1. This energy gain readily guarantees that the first-order transition occurs at a temperature higher than that of a continuous transition to the single- $\mathbf{q}$  state in the simple Landau analysis. This sTQ state indeed has a four-sublattice *partial order* with  $\{\phi_{\mathbf{r}}\} = \{\mathbf{0}, \phi\mathbf{v}_1^+, \phi\mathbf{v}_2^+, \phi\mathbf{v}_3^+\}$  as shown in Fig. 1(c). The four

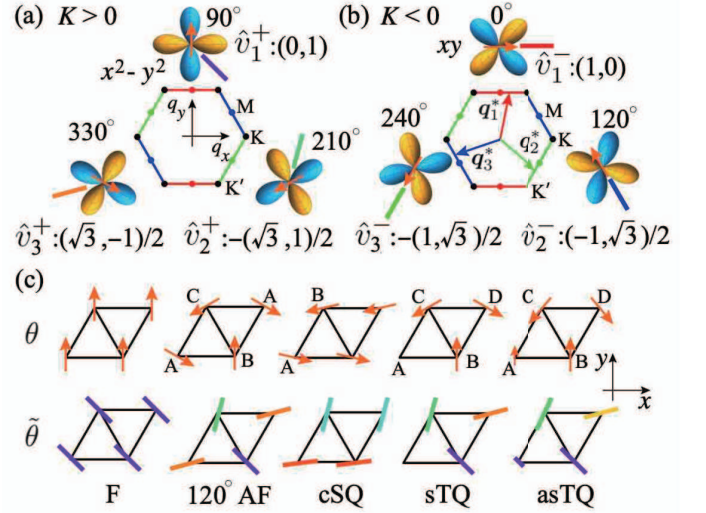


FIG. 1: Lowest-energy eigenmode  $\phi(\mathbf{q}^*)$  of  $\mathcal{H}_{\text{ex}}$  for  $\mathbf{q}_{\ell}^*$  on the BZ edges for (a)  $K > 0$  and (b)  $K < 0$ . Within each edge, the eigenmode does not change and the orbital form is illustrated together with the corresponding pseudo spin (arrow for angle  $\theta$ ) and nematic director (bar for angle  $\tilde{\theta} = -\frac{1}{2}\theta$ ). (c) Representative configuration of commensurate orders. Arrows represent the pseudo spins (1). Bars represent the directors  $\hat{e}(\tilde{\theta})$ , which are directionless. A–D are the sublattice indices.

sets of  $\{\sigma_{\ell}\}$  correspond to domains with the disordered site on different sublattices.

For  $5K < 2J < 0$ , one may expect a similar sTQ state, but the situation is quite different. Employing Eq. (4) with  $\mathbf{v}_{\ell}^+ \rightarrow \mathbf{v}_{\ell}^-$  results in  $V = 0$ . Thus, the sTQ state is not stable for  $K < 0$  in contrast to the case of  $K > 0$ .

*Parasitic ferro moments.*—The cubic term (2) affects the order parameters significantly. Using the eigenmodes  $\mathbf{v}_{\ell}^+$  for  $K > 0$ , we find that  $V$  contains the following term

$$-\frac{3}{2}\lambda\mathbf{D} \cdot \phi(\mathbf{0}), \quad \mathbf{D} = (\sqrt{3}(\phi_3^2 - \phi_2^2), 2\phi_1^2 - \phi_2^2 - \phi_3^2). \quad (5)$$

Once the symmetry  $\phi_1 = \phi_2 = \phi_3$  is broken,  $\mathbf{D}$  is activated and this induces the ferro moment  $\phi(\mathbf{0})$ <sup>49,50</sup>. This is natural since in the sTQ state  $\phi_{\mathbf{r}}$ 's are disordered at a quarter of the sites and thus this state is not stable at  $T = 0$ . Such an asymmetric triple- $\mathbf{q}$  (asTQ) state is illustrated in Fig. 1(c) for the case of  $\phi_1 > \phi_2 = \phi_3$ , and  $\phi(\mathbf{0}) \parallel \hat{e}(\frac{\pi}{2})$ . In general, the  $\mathbf{v}_{\ell}^+$  and  $\mathbf{v}_{\ell}^-$  components hybridize, and this rotates  $\phi_{\mathbf{r}}$ . See  $\phi_{\mathbf{r}}$  in the C and D sublattice in Fig. 1(c) in Appendix A.

Even for single- $\mathbf{q}$  states, such a ferroic moment emerges. Consider the single- $\mathbf{q}$  state for  $K < 0$  with  $\mathbf{q}^* = \mathbf{Q}_{\ell}$ . The AF mode  $\phi(\mathbf{Q}_{\ell}) \equiv \phi_{\ell} \hat{e}(\theta_{\ell})$  can couple with the ferro mode  $\phi(\mathbf{0}) = \phi_0 \hat{e}(\theta_0)$ , and this yields  $V \sim 3N\lambda\phi_{\ell}^2\phi_0 \sin(2\theta_{\ell} + \theta_0)$ . This shows that the ferro component  $\phi(\mathbf{0})$  points to the direction  $\theta_0 = \frac{3}{2}\pi - 2\theta_{\ell}$ , and thus, the canted single- $\mathbf{q}$  (cSQ) state is stabilized as shown in Fig. 1(c). For  $K < 0$ ,  $\theta_{\ell} = (\ell - 1)\omega$ , and thus,  $\phi(\mathbf{0}) \parallel \hat{e}((-\frac{7}{4} + \ell)\omega)$ .

*IC triple- $\mathbf{q}$ .*—Now, we study the triple- $\mathbf{q}$  states for  $K > 0$  with  $\{\mathbf{q}_{\ell}^*\}_{\ell=1}^3$  on the BZ edges. Note that those for  $K < 0$  gains no

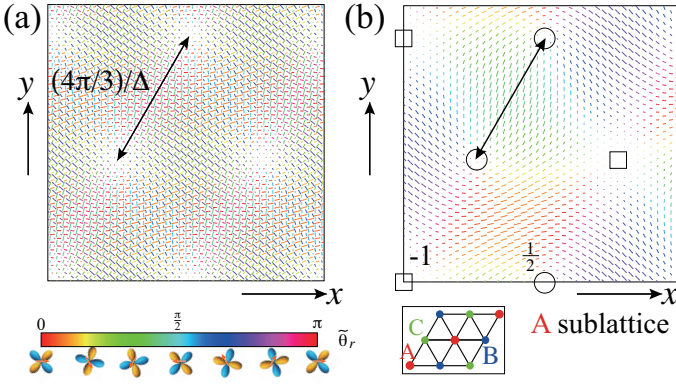


FIG. 2: (a) Director angle configuration  $\tilde{\theta}_r$  in the triple- $q$  state with  $\mathbf{q}_\ell^* \sim \mathbf{q}_{K'} - \Delta \hat{e}_{4-\ell}$  with  $\Delta = \frac{\pi}{24}$ . (b) The A-sublattice structure of (a). The vortices (square) are located at the center of the half-vortices (circle) honeycomb structure. The distance between the two half-vortices is shown by double-headed arrows.

energy in  $V$ . Since  $-\mathbf{q}_\ell^* \neq \mathbf{q}_\ell^*$ , the factor  $\sigma_\ell \cos(\mathbf{Q}_\ell \mathbf{r})$  in Eq. (4) should be replaced by  $\cos(\mathbf{q}_\ell^* \cdot \mathbf{r} + \eta_\ell)$  with a general phase  $\eta_\ell$ . Then,  $V = -\frac{3}{4} N \lambda \phi_1 \phi_2 \phi_3 \cos(\eta_1 + \eta_2 + \eta_3)$  and this is minimized when  $\eta_1 + \eta_2 + \eta_3 \equiv 0$ . This energy gain guarantees that the IC triple- $q$  (IC-TQ) state is more stable than the single- $q$  state for sufficiently large  $\lambda$ .

Such triple- $q$  configurations can be visualized as *orbital moiré*. Figure 2(a) shows an example of “nematic” director angles  $\tilde{\theta}_r \equiv -\frac{1}{2}\theta_r \pmod{\pi}$ . They point to the direction of the orbital node:  $\tilde{\theta}_r = 0$  for the  $xy$ -orbital and  $\frac{3}{4}\pi$  for  $x^2 - y^2$ . When  $\mathbf{q}_\ell^*$ 's are near the K or  $K'$  point, the configuration is characterized by a set of sublattice directors  $\tilde{\theta}_{r \in X}$  ( $X=A, B$ , or  $C$ ). Then, we introduce their vector vortex charges  $\mathbf{n} = (n_A, n_B, n_C)$  defined by<sup>51</sup>

$$n_X(\mathbf{r}) \equiv \oint_{\mathbf{r}+\mathbf{r}' \in X} \frac{d\mathbf{r}'}{2\pi} \cdot \frac{\partial}{\partial \mathbf{r}'} \tilde{\theta}_{\mathbf{r}+\mathbf{r}'}, \quad (6)$$

where the integral is defined for a closed loop around the site  $\mathbf{r}$ . For the data in Fig. 2, the ordering vectors are chosen as  $\mathbf{q}_\ell^* = \mathbf{q}_{K'} - \Delta \hat{e}_{4-\ell}$  with  $\Delta = \frac{\pi}{24}$ . The panel (a) shows the  $\tilde{\theta}_r$  configuration and vortices and half-vortices form a triangular lattice with the approximate periodicity  $4\pi/(3\Delta)$ . Their vector vortex charges are either  $\mathbf{n}_1 = (-1, \frac{1}{2}, \frac{1}{2})$ ,  $\mathbf{n}_2 = (\frac{1}{2}, -1, \frac{1}{2})$ , or  $\mathbf{n}_3 = (\frac{1}{2}, \frac{1}{2}, -1)$ . The panel (b) shows the director configuration in the A-sublattice. One can easily see that half-vortices ( $n_A = \frac{1}{2}$ ) form a honeycomb structure with vortices ( $n_A = -1$ ) being located at the center of the hexagon. Similarly, when  $\mathbf{q}_\ell^*$ 's are close to the M points, the moiré texture is characterized by four-sublattice vortices. See Appendix C.

*Monte Carlo simulation.*—We have performed classical Monte Carlo (MC) simulations to examine the effects of thermal fluctuations on the triple- $q$  orders discussed above. We have used hexagonal clusters with the edge length  $L \leq 96$  and the maximum one has  $N=27937$  sites. The periodic boundary conditions are applied for the three pairs of opposite edges. We use exchange MC algorithm<sup>52,53</sup> combined with single-“spin”

flip updates for efficient simulations. At each temperature  $T$ , we calculate observables by averaging over  $M = 10^6$  MC steps (MCS) after thermalization of typically  $10^5$  MCS. We parameterize  $(J, K) = \bar{J}(\cos \alpha, \sin \alpha)$  with  $\bar{J} = 1$ .

Let  $\{\phi_r^{(m)}\}$  denote the snapshot at the  $m$ -th MCS and define their Fourier component by  $\phi_\sigma^{(m)}(\mathbf{q}_\ell) \equiv N^{-1} \sum_r v_\ell^\sigma \cdot \phi_r^{(m)} e^{-i\mathbf{q}_\ell \cdot \mathbf{r}}$  ( $\sigma = \pm$ ) for those  $\mathbf{q}_\ell$ 's on the  $\ell$ -th BZ edge. Since  $\phi_\sigma^{(m)}(\mathbf{q}_\ell)$ 's may have arbitrary phases, we define the single- $q$  order parameter as  $S^\sigma(\mathbf{q}_\ell) := M^{-1} \sum_m |\phi_\sigma^{(m)}(\mathbf{q}_\ell)|^2 =: \langle |\phi_\sigma(\mathbf{q}_\ell)|^2 \rangle$ , while that for the triple- $q$  order is defined as  $\mathcal{T}^\sigma(\{\mathbf{q}_\ell\}_{\ell=1}^3) \equiv \langle \phi_\sigma(\mathbf{q}_1) \phi_\sigma(\mathbf{q}_2) \phi_\sigma(\mathbf{q}_3) \rangle$  with  $\mathbf{q}_1 + \mathbf{q}_2 + \mathbf{q}_3 \equiv 0$ .

Figure 3(a) shows the  $T$ - $\alpha$  phase diagram for  $\lambda = 1$ . Similar results have been obtained for  $\lambda \gtrsim 0.5$ . There appear six ordered phases in total. Their transition temperature is mostly determined as the temperature where the Binder ratio of the order parameter coincides for  $L = 32$  and  $48$ . For first-order transitions, it is identified to the temperature at which the order parameter jumps upon lowering  $T$ . Near  $\alpha = 0$ , the  $120^\circ$  AF order is stable and its transition from the high- $T$  disordered phase is first order. For the F and cSQ states, the finite-size scaling analysis shows that the transition is of the three-state Potts universality class as shown in Appendix C. For the sTQ, we find that the universality class of the transition belongs to that at the critical line of the Ashkin-Teller model<sup>54</sup>. This is apparent in both triple- $q$   $\mathcal{T}^+(\{\mathbf{Q}_\ell\}_{\ell=1}^3)$  and single- $q$   $S^+(\mathbf{Q}_\ell)$  order parameters as shown in Fig. 3(b) for  $\alpha = 0.375\pi$ . The critical exponents determined are  $\nu \simeq 0.71$  and  $\beta = \nu/8$ , where the latter relation holds along the critical line. As  $\alpha$  varies,  $\nu$  changes slightly, but its value is close to that for the four-state Potts universality class corresponding to the end point of the critical line:  $\nu = \frac{2}{3}$  and  $\beta = \frac{1}{12}$ <sup>55,56</sup>. These results are related to the four-fold degeneracy of the disordered site position. Similar situation has been discussed in the literature for such an example of  $N_2$  molecules adsorbed on Kr-plated graphite<sup>57,58</sup>. Between the sTQ and  $120^\circ$ -AF states, the IC-TQ appears at finite  $T$ . However, it becomes unstable at lower  $T$ 's since a finite density of disordered sites has no contribution to energy gain. Note that the “incommensurate” is just nominal and means  $\mathbf{q}^*$  is neither on the K( $K'$ ) nor M point along the edge of the BZ.

*IC-TQ and orbital moiré.*— In the IC-TQ state, the ordering vector  $\mathbf{q}^*$  moves along the BZ edge with lowering  $T$ , and this is similar to the case of the Devil's staircase in frustrated magnets<sup>59</sup>. The varying  $\mathbf{q}^*$  is triggered by forming dislocations of the vortex lattice as shown in Appendix C. Figure 3(c) shows a snapshot sublattice configuration of  $\tilde{\theta}_r$ , averaged over 1000 MCS. It is well described by a hexagonal moiré texture with its sublattice vortices  $n_A = -1$  and  $\frac{1}{2}$  (Fig. 2). The short-time averaging makes the vortex cores clearer than in a single snapshot. For  $\alpha \lesssim \tan^{-1} \frac{2}{3} \simeq \alpha_c$ , the  $120^\circ$  AF order seems to appear at the lowest temperature. Near  $\alpha = \alpha_c$ , the MC sampling is not sufficient due to the presence of many local minima related to the IC configurations. We expect  $\mathbf{q}^*$  approach  $\mathbf{q}_{K, K'}$  and the IC-TQ states are unstable at lower temperatures. These IC-TQ states intervene between the sTQ and the asTQ states for  $\alpha \gtrsim \alpha_c$ . However, we should be aware that the vector  $\mathbf{q}^*$  depends on  $L$  and the boundary con-

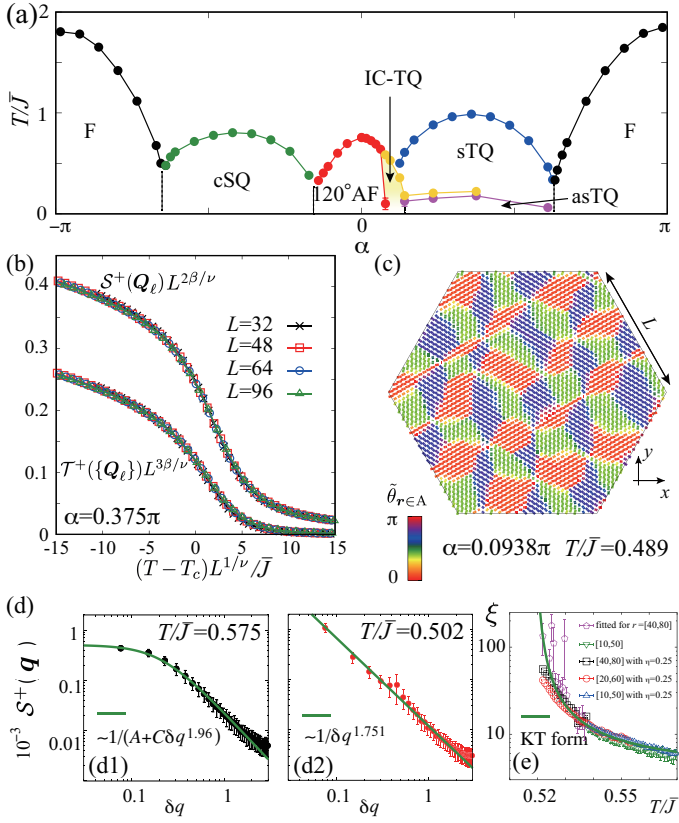


FIG. 3: (a)  $T$ - $\alpha$  phase diagram. The low- $T$  region of the IC-TQ state between the  $120^\circ$  and the sTQ states is expected to be the  $120^\circ$ -AF one because  $\mathbf{q}^*$  moves to  $\mathbf{q}_{K,K'}$  as  $T$  decreases. (b) Finite-size scaling analysis of  $S^+(\mathbf{Q}_\ell)$  and  $\mathcal{T}^+(\{\mathbf{Q}_\ell\})$  for  $\alpha = 0.375\pi$  with  $(\nu, \beta) = (0.71, 0.089)$ , where the transition temperature is  $T_c/\bar{J} \simeq 0.9853$ . (c) Snapshot  $\tilde{\theta}_r$  in the A-sublattice for  $L = 50$ ,  $\alpha = 0.0938\pi$  and  $T/\bar{J} = 0.489$ , where the IC-TQ configuration with  $\mathbf{q}_\ell^* = \mathbf{q}_{K'} - \frac{4\pi}{3} \frac{3}{50} \hat{e}_{4-\ell}$  is realized. (d)  $S^+(\mathbf{q})$  vs  $\delta\mathbf{q} = \mathbf{q} - \mathbf{q}^*$  for (d1)  $T > T^*$  and (d2)  $T < T^*$  for  $L = 96$ , where the data along two directions  $\delta\mathbf{q} \parallel \hat{e}(\ell\omega)$  and  $\parallel \hat{e}((\ell - \frac{1}{4})\omega)$  are averaged. The data are fitted in the region of  $0.5 \leq |\delta\mathbf{q}| \leq 2.0$  by a function shown in the figure. (e)  $T$  dependence of correlation length  $\xi$  for  $L = 96$  obtained by fitting  $\chi_{uu}(r\hat{e}_0)$  with parameters  $c_{1,2,3}$ ,  $\chi_{uu}(r\hat{e}_0) = c_1 \cos[(c_2 + \omega)r] r^{-c_3} e^{-r/\xi}$  for  $10 \leq r \leq 50$  (blue, green) for higher  $T$  and  $20 \leq r \leq 60$  (red) and  $40 \leq r \leq 80$  (black, pink) for lower  $T$ . The green curve is the KT form  $\xi = a_1 \exp[a_2/\sqrt{T - T^*}]$  with  $a_{1,2}$  being a constant. Data fitted with fixed  $c_3 = 1/4$  (expected in the KT form) and those with  $c_3$  being a free parameter are similar, while the low- $T$  data for the latter have large error bars (pink).

ditions for these IC-TQ states. Recalling that the phases  $\eta_\ell$ 's correspond to the choice of the origin of IC order<sup>29</sup>, it is natural to expect their fluctuations destroy the IC long range order<sup>24,60-62</sup>. Indeed, one evidence of such a quasi-long-range order is the power-law behavior of the correlation function of  $\phi(\mathbf{q})$  shown in Fig. 3(d), where the mass term  $A$  in  $S^+(\mathbf{q}) \sim (A + C|\mathbf{q} - \mathbf{q}^*|^2)^{-1}$  vanishes below the transition temperature

$T^*/\bar{J} \simeq 0.518$ . The dependence on  $\delta\mathbf{q} = \mathbf{q} - \mathbf{q}^*$  is obtained by fitting the data for  $0.5 < |\delta\mathbf{q}| < 2.0$  near  $T^*$ , resulting in  $S^+(\mathbf{q}) \sim |\delta\mathbf{q}|^{-\zeta}$  with  $\zeta \simeq 1.6 \sim 2.0$ . See Appendix C. These are not far from the value  $\zeta = 2 - 1/4 = 1.75$  at the KT transition<sup>24</sup>. The real space correlation  $\chi_{ij}(\mathbf{r}) = \langle \phi_{i,r} \phi_{j,0} \rangle$  shows an exponential decay above  $T^*$ . Figure 3(e) shows that its correlation length  $\xi$  is well fitted by the exponential divergence typical in the case of the KT transition as  $\xi \propto \exp[\text{const.}/\sqrt{T - T^*}]$ . See Appendix C. In addition, the data of  $\mathcal{T}^+$  indicate that all the configurations of  $\{\eta\}$  are realized, which leads to a relation  $\langle \phi'_+(\mathbf{q}_1) \phi'_+(\mathbf{q}_2) \phi'_+(\mathbf{q}_3) \rangle = -\langle \phi'_+(\mathbf{q}_1) \phi''_+(\mathbf{q}_2) \phi''_+(\mathbf{q}_3) \rangle$ . Here,  $\phi'$  ( $\phi''$ ) denotes the real (imaginary) part of  $\phi$ . In this sense the phases  $\{\eta\}$  are not locked as shown in Appendix C.

*Discussions.*—Let us discuss how to detect the predicted quadrupolar orders. Below, we assume that the system has a weak three-dimensionality with a uniform stacking of  $\phi_r$  along the  $z$  axis and the IC-TQ states have true long-range orders. The most direct and powerful method effective for the quadrupole orders is the resonant x-ray scattering experiments<sup>63,64</sup>. The sTQ order is identified by observing disordered sites and one can use nuclear magnetic or quadrupole resonance for that purpose if appropriate nuclei exist as has been discussed for  $\text{UNi}_4\text{B}$ <sup>46</sup>. One can also detect free quadrupole moments at the disordered sites by ultrasonic experiments. When quadrupole order parameter spatially modulates<sup>65</sup>, an electric polarization field  $\mathbf{P}(\mathbf{r})$  is induced in proportion to  $\boldsymbol{\pi}(\mathbf{r}) \equiv (\partial_x \phi_{u,r} + \partial_x \phi_{v,r}, \partial_x \phi_{u,r} - \partial_y \phi_{v,r}, 0)$  and it is detectable. See a recent observation of polar skyrmions in  $\text{PbTiO}_3/\text{SrTiO}_3$ <sup>66</sup>.

When the system has itinerant electrons, they feel a moiré of ordered quadrupoles. This should be reflected in the band structure and Moiré minibands are recently observed in twisted bilayer  $\text{WSe}_2$  by the resonant inelastic light scattering experiment<sup>67</sup>. Since the IC-TQ order lacks the local inversion symmetry, one expects that the spin-orbit coupling is activated, and it transcribes the orbital texture into a moiré of magnetizations  $\mathbf{M}(\mathbf{r})$ . It is induced by electric current  $\mathbf{j}$  via the interaction energy

$$\Delta E = g_1 (\mathbf{M}_q \times \boldsymbol{\pi}_{-q})_z j_z + g_2 M_{zq} (\boldsymbol{\pi}_{-q} \times \mathbf{j})_z, \quad (7)$$

where  $g_1$  and  $g_2$  are constants.  $\boldsymbol{\pi}_q$  and  $\mathbf{M}_q$  are the Fourier transform of  $\boldsymbol{\pi}(\mathbf{r})$  and  $\mathbf{M}(\mathbf{r})$ , respectively. In this Letter we have not considered magnetic degrees of freedom such as magnetic dipole  $M_z(\mathbf{r})$  perpendicular to the triangular plane, and octupole moments  $\sim M_x(\mathbf{r})[M_x^2(\mathbf{r}) - 3M_y^2(\mathbf{r})]$  or  $M_y(\mathbf{r})[M_y^2(\mathbf{r}) - 3M_x^2(\mathbf{r})]$ . If they exist, they may order around the cores of quadrupole vortices and the overall configuration is a hybrid quadrupole-dipole/octupole skyrmion(-like) lattice. Such a dipole-quadrupole skyrmion has been proposed for a spin-1 system with an elevated  $\text{SU}(3)$  symmetry<sup>68</sup>. See also recent analyses<sup>69-73</sup>. Entropy release of the magnetic degrees of freedom is large at the sites with disordered quadrupole and it helps such exotic phases to persist even at low temperatures, as demonstrated for multiple- $\mathbf{q}$  multipole orders<sup>44,46,74</sup>. Searching for such states is one of fascinating directions in future.

*Summary.*—We have proposed a minimal quadrupole model which realizes orbital moiré texture on the triangular lattice. This model exhibits various triple- $\mathbf{q}$  orders and they are stabilized by the cubic anisotropy that is forbidden in magnetic

systems due to the time-reversal symmetry. We have shown the emergence of incommensurate triple- $\mathbf{q}$  states that exhibits an orbital moiré texture with quasi-long-range order. We expect our results pave a basis for the future investigation for nonmagnetic multiple- $\mathbf{q}$  and moiré physics.

*Acknowledgement.*—This work was supported by a Grant-in-Aid for Scientific Research (Grant Nos. JP21H01031, JP23K20824, and JP23H04869) from the Japan Society for the Promotion of Science.

### Appendix A: Eigenmodes of exchange interaction

Let us analyze the exchange coupling  $\mathcal{H}_{\text{ex}}$  in Eq. (3) in the main text. The Fourier bases  $\phi(\mathbf{q})$  are defined as

$$\phi(\mathbf{q}) = \frac{1}{N} \sum_r e^{-i\mathbf{q}\cdot\mathbf{r}} \phi_r, \quad \phi_r = \sum_{\mathbf{q}} e^{i\mathbf{q}\cdot\mathbf{r}} \phi(\mathbf{q}), \quad (\text{A1})$$

where  $N$  is the site number.  $\mathcal{H}_{\text{ex}}$  is written with them as

$$\mathcal{H}_{\text{ex}} = \frac{N}{2} \sum_{\mathbf{q}} \phi^\dagger(\mathbf{q}) \cdot \hat{\mathcal{J}}_{\mathbf{q}} \phi(\mathbf{q}), \quad \phi(\mathbf{q}) \equiv \begin{bmatrix} \phi_u(\mathbf{q}) \\ \phi_v(\mathbf{q}) \end{bmatrix}, \quad (\text{A2a})$$

with

$$\hat{\mathcal{J}}_{\mathbf{q}} \equiv \begin{pmatrix} J\gamma_{\mathbf{q}} + K\gamma'_{\mathbf{q}} & K\zeta_{\mathbf{q}} \\ K\zeta_{\mathbf{q}} & J\gamma_{\mathbf{q}} - K\gamma'_{\mathbf{q}} \end{pmatrix}, \quad (\text{A2b})$$

$$\gamma_{\mathbf{q}} \equiv 2 \cos q_x + 4 \cos \frac{q_x}{2} \cos \frac{\sqrt{3}q_y}{2}, \quad (\text{A2c})$$

$$\gamma'_{\mathbf{q}} \equiv 2 \cos q_x - 2 \cos \frac{q_x}{2} \cos \frac{\sqrt{3}q_y}{2}, \quad (\text{A2d})$$

$$\zeta_{\mathbf{q}} \equiv 2\sqrt{3} \sin \frac{q_x}{2} \sin \frac{\sqrt{3}q_y}{2}, \quad (\text{A2e})$$

where the  $\mathbf{q}$ -sum runs over the first Brillouin zone (1BZ) of the triangular lattice. The eigenvalues of  $\hat{\mathcal{J}}_{\mathbf{q}}$  are denoted as  $J_{\mathbf{q}}^\pm$  and are calculated as

$$J_{\mathbf{q}}^\pm = J\gamma_{\mathbf{q}} \pm |K| \sqrt{\gamma_{\mathbf{q}}'^2 + \zeta_{\mathbf{q}}^2}. \quad (\text{A3})$$

Let  $\mathbf{q}^*$  denotes the wavevector where the eigenvalue  $J_{\mathbf{q}}^-$  has the negatively largest value. For  $J > 0$ , one easily finds that  $\mathbf{q}^*$  locates at  $(\Delta_M, 2\pi/\sqrt{3})$  or its equivalent positions in the 1BZ, and the parameter  $\Delta_M$  is

$$\Delta_M = \begin{cases} 0 & (|K| > \frac{2J}{5} > 0) \\ 2 \cos^{-1} \left[ \frac{2J + |K|}{4(J - |K|)} \right] & (|K| \leq \frac{2J}{5}) \end{cases}, \quad (\text{A4})$$

and  $\mathbf{q}^* = (\frac{2\pi}{3}, \frac{2\pi}{\sqrt{3}}) = \mathbf{q}_{K'}$  at  $|K| = 0$ . When the system undergoes a second-order phase transition to an ordered state,  $\mathbf{q}^*$  is expected to be its ordering vector. Note that the  $\mathbf{q}^*$  moves from  $\pm\mathbf{q}_{K'}$  to the M point  $\mathbf{Q}_1 = (0, \frac{2\pi}{\sqrt{3}})$  or its equivalent one along the 1BZ boundary as  $|K|$  increases. The eigenvector at  $\mathbf{q}^*$  corresponds to the order parameter of the incommensurate states. There are six independent wave vectors:  $\pm\mathbf{q}_\ell^*$  ( $\ell = 1, 2, 3$ ):

$$\mathbf{q}_1^* = \left(0, \frac{2\pi}{\sqrt{3}}\right) + \Delta_M(1, 0) \equiv \mathbf{Q}_1 + \Delta_M \hat{e}_0, \quad (\text{A5a})$$

$$\mathbf{q}_2^* = \left(\pi, -\frac{\pi}{\sqrt{3}}\right) + \Delta_M \left(-\frac{1}{2}, -\frac{\sqrt{3}}{2}\right) \equiv \mathbf{Q}_2 + \Delta_M \hat{e}_2, \quad (\text{A5b})$$

$$\mathbf{q}_3^* = \left(-\pi, -\frac{\pi}{\sqrt{3}}\right) + \Delta_M \left(-\frac{1}{2}, \frac{\sqrt{3}}{2}\right) \equiv \mathbf{Q}_3 + \Delta_M \hat{e}_1, \quad (\text{A5c})$$

with  $-2\pi/3 \leq \Delta_M \leq 2\pi/3$ . The unit vectors are defined as  $\hat{e}_\ell \equiv \hat{e}(\ell\omega)$ , where  $\hat{e}(\theta) \equiv (\cos \theta, \sin \theta)$  and  $\omega \equiv \frac{2\pi}{3}$ . See Eq. (1) in the main text. The eigenvectors  $\hat{v}_\ell^\pm$  satisfy

$$\hat{\mathcal{J}}_{\mathbf{q}_\ell^*} \mathbf{v}_\ell^\pm = \left\{ J\gamma_{\mathbf{q}_\ell^*} \mp 2K \left[ \cos \Delta_M + \cos \left( \frac{\Delta_M}{2} \right) \right] \right\} \mathbf{v}_\ell^\pm, \quad (\text{A6})$$

where  $\cos \Delta_M + \cos(\Delta_M/2) \geq 0$ . They are given by

$$\mathbf{v}_1^- = (1, 0)^\text{T} = \hat{e}_0, \quad \mathbf{v}_1^+ = (0, 1)^\text{T} = \hat{e}(\frac{3\omega}{4}), \quad (\text{A7a})$$

$$\mathbf{v}_2^- = (-\frac{1}{2}, \frac{\sqrt{3}}{2})^\text{T} = \hat{e}_1, \quad \mathbf{v}_2^+ = -(\frac{\sqrt{3}}{2}, \frac{1}{2})^\text{T} = \hat{e}(\frac{7\omega}{4}), \quad (\text{A7b})$$

$$\mathbf{v}_3^- = (-\frac{1}{2}, -\frac{\sqrt{3}}{2})^\text{T} = \hat{e}_2, \quad \mathbf{v}_3^+ = (\frac{\sqrt{3}}{2}, -\frac{1}{2})^\text{T} = \hat{e}(\frac{11\omega}{4}). \quad (\text{A7c})$$

The eigenmodes of the leading instability for  $K > 0$  are  $\mathbf{v}_\ell^+$ 's, while  $\mathbf{v}_\ell^-$ 's for  $K < 0$ . Note that the sign of  $2K$  in the RHS of Eq. (A6) is not “ $\pm$ ” but represents the leading mode corresponding to  $\text{sgn}(K)$ .

For  $J < 0$ , one can find

$$\mathbf{q}^* = \begin{cases} \mathbf{0} & (|K| < -2J) \\ \mathbf{Q}_\ell & (\ell = 1, 2, 3) \quad (|K| > -2J) \end{cases}. \quad (\text{A8})$$

Note that  $J_{\mathbf{q}^*}^+ = J_{\mathbf{q}^*}^-$  for  $\mathbf{q}^* = \mathbf{0}$  and the eigenvectors are arbitrary. Typical examples of the dispersion  $J_{\mathbf{q}}^\pm$  are shown in Fig. 4.

### Appendix B: Landau Free energy

In this Appendix, we will derive the Landau free energy for several phases appeared in the main text. We will not show the details of minimization procedure for simplicity but the line of discussion is similar to that for cubic systems<sup>49,50</sup>.

The free energy up to the fourth order in  $\phi$ 's is given as

$$F = \frac{N}{2} \sum_{\mathbf{q}} \phi^\dagger(\mathbf{q}) \left( a_0 + \hat{\mathcal{J}}_{\mathbf{q}} \right) \phi(\mathbf{q}) + \sum_r \left[ \lambda \left( 3\phi_{u,r}^2 - \phi_{v,r}^2 \right) \phi_{v,r} + c |\phi_r|^4 + \dots \right], \quad (\text{B1})$$

where  $a_0 = \bar{a}_0 T$  with  $T$  being temperature, and  $\bar{a}_0$ ,  $\lambda$ ,  $c$  are positive constants.

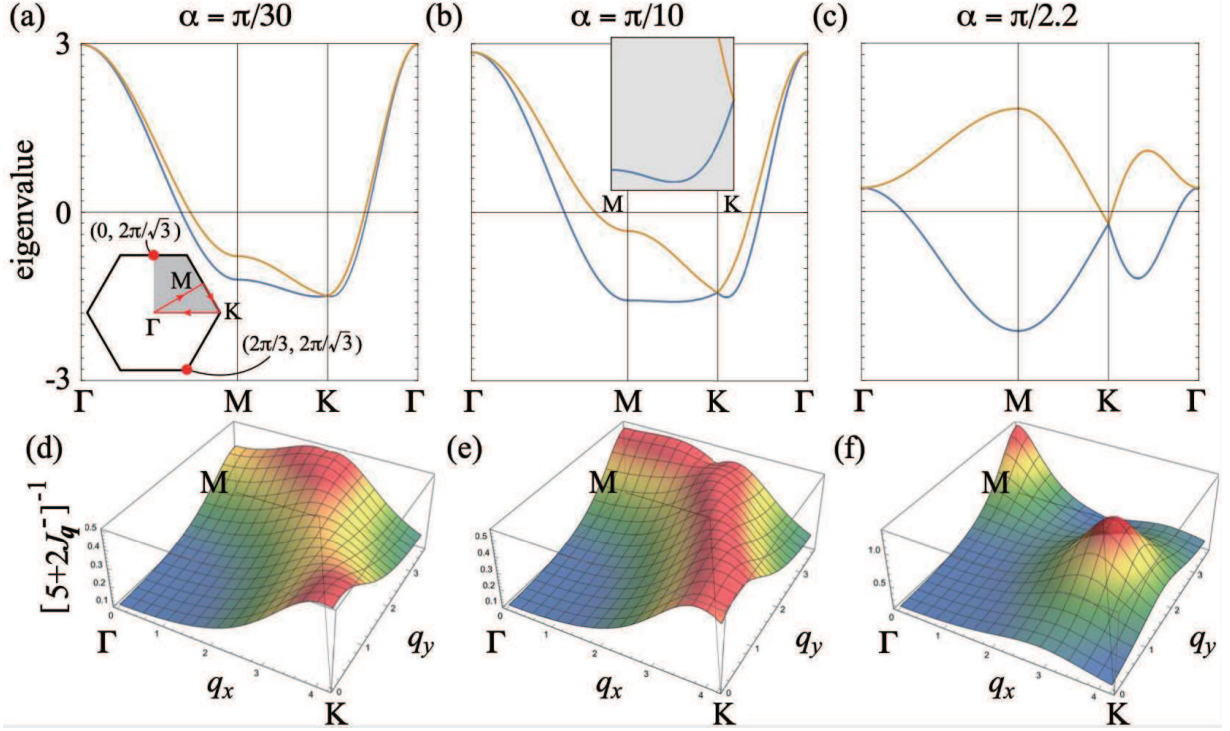


FIG. 4: (a)-(c) Two eigenvalues  $J_q^-$  (blue) and  $J_q^+$  (red) along the high symmetry axes in the 1BZ. The parameters are  $(J, K) = (\cos \alpha, \sin \alpha)$ . The inset in (a) shows the 1BZ, while the inset in (b) is a zoom up of the region between the M and the K points. (d)-(f)  $1/(5 + 2J_q^-)$  for the data in (a)-(c), respectively.

In the following, we assume the ordering vectors are  $\mathbf{q}_\ell^*$  ( $\ell = 1, 2, 3$ ), which are either commensurate  $\mathbf{Q}_\ell$  or incommensurate (IC) ones on the 1BZ boundary. Taking into account the mode-mode coupling terms arising from the cubic term, one finds that  $\phi(\mathbf{0})$  couples with  $\phi(\mathbf{q}_\ell^*)$  in the linear order in  $\phi(\mathbf{0})$ . The other modes in the cubic term just appear at least in the quadratic orders and are safely ignored. As for the mode-mode coupling terms in the fourth-order terms, the terms proportional to  $c$  are proportional to the third order in the triple- $\mathbf{q}$  order parameters, which are subleading one compared to the terms arising from the cubic term proportional to  $\lambda$ . Indeed, when  $|\phi(\mathbf{q}_\ell^*)|$  is  $\ell$ -independent, they vanish.

First, let us consider the commensurate cases with  $\mathbf{q}_\ell^* = \mathbf{Q}_\ell$ :  $\phi(\mathbf{Q}_\ell) = \sigma_\ell \phi_\ell \mathbf{v}_\ell^s$  ( $\sigma_\ell = \pm 1$ ,  $\phi_\ell \geq 0$ ,  $s = +$  or  $-$ ), which couples with  $\phi(\mathbf{0})$ . The free energy  $F = F_s$  is given by

$$\frac{F_s}{N} = \frac{1}{2} \sum_{\ell=1,2,3} (a_0 + J_{\mathbf{Q}_\ell}^-) \phi_\ell^2 - 6\lambda \sigma_1 \sigma_2 \sigma_3 \phi_1 \phi_2 \phi_3 \delta_{s,+} + \frac{c}{2} \left[ 3(\phi_1^2 + \phi_2^2 + \phi_3^2)^2 - \sum_{\ell=1,2,3} \phi_\ell^4 \right] - \frac{3s\lambda}{2} \mathbf{D} \cdot \phi(\mathbf{0}). \quad (\text{B2})$$

Here, we have kept terms linear in  $\phi(\mathbf{0})$  and

$$\mathbf{D} \equiv \begin{bmatrix} \sqrt{3}(-\phi_2^2 + \phi_3^2) \\ 2\phi_1^2 - \phi_2^2 - \phi_3^2 \end{bmatrix} = 2 \sum_{\ell=1,2,3} \phi_\ell^2 \mathbf{v}_\ell^+. \quad (\text{B3})$$

When the leading ordering vectors are IC  $\mathbf{q}_\ell^*$ 's, they are distinct from  $-\mathbf{q}_\ell^*$  and we replace  $\phi(\mathbf{Q}_\ell)$  by

$$\phi(\mathbf{q}_\ell^*) = \phi_\ell e^{i\eta_\ell} \mathbf{v}_\ell^s, \quad \phi(-\mathbf{q}_\ell^*) = [\phi(\mathbf{q}_\ell^*)]^*. \quad (\text{B4})$$

Then, the free energy  $F = F_s^{\text{IC}}$  becomes

$$\frac{F_s^{\text{IC}}}{N} = \sum_{\ell=1,2,3} (a_0 + J_{\mathbf{q}_\ell^*}^-) \phi_\ell^2 - 12\lambda \phi_1 \phi_2 \phi_3 \cos \eta_{\text{tot}} \delta_{s,+} + 6c(\phi_1^2 + \phi_2^2 + \phi_3^2)^2 - 3s\lambda \mathbf{D} \cdot \phi(\mathbf{0}), \quad (\text{B5})$$

where  $\eta_{\text{tot}} = \eta_1 + \eta_2 + \eta_3$ .

### 1. Single- $\mathbf{q}$ states

We now consider the free energy density of the single- $\mathbf{q}$  states. The results for commensurate and IC cases are

$$\frac{F_{s\ell}}{N} = \frac{1}{2} (a_0 + J_{\mathbf{Q}_\ell}^-) \phi_\ell^2 + c \phi_\ell^4 - 3s\lambda \phi_\ell^2 \mathbf{v}_\ell^+ \cdot \phi(\mathbf{0}), \quad (\text{B6})$$

$$\frac{F_{s\ell}^{\text{IC}}}{N} = (a_0 + J_{\mathbf{q}_\ell^*}^-) \phi_\ell^2 + 6c \phi_\ell^4 - 6s\lambda \phi_\ell^2 \mathbf{v}_\ell^+ \cdot \phi(\mathbf{0}), \quad (\text{B7})$$

respectively. Here, we have used Eq. (B4) for deriving Eq. (B7). We rescale the order parameters as  $\phi_\ell = \varphi_\ell / \sqrt{2}$  in  $F_{s\ell}^{\text{IC}}$ . Then, we obtain

$$\frac{F_{s\ell}^{\text{IC}}}{N} = \frac{1}{2} (a_0 + J_{\mathbf{q}_\ell^*}^-) \varphi_\ell^2 + \frac{3c}{2} \varphi_\ell^4 - 3s\lambda \varphi_\ell^2 \mathbf{v}_\ell^+ \cdot \phi(\mathbf{0}). \quad (\text{B8})$$

Note that the fourth-order term in  $F_{s\ell}^{\text{IC}}$  [Eq. (B8)] is larger than that in  $F_{s\ell}$  [Eq. (B6)], and this represents the commensurate

locking. See Sec. E. It is clear that once  $\varphi_\ell$  or  $\phi_\ell$  is finite, the ferroic moment  $\phi(\mathbf{0})$  is induced along the direction of  $sv_\ell^+$  for  $\lambda > 0$ , which we have named canted SQ state (cSQ). This kind of induction of uniform moment is common in the quadrupole systems of ‘‘E’’-type (two-dimensional irrep.)<sup>49,50,75,76</sup>.

## 2. Symmetric triple-q state for $K > 0$

Let us discuss the symmetric triple- $\mathbf{q}$  (sTQ) state with  $\mathbf{Q}_\ell$ 's for  $K > 0$ . As explained in the main text, this state is a symmetric superposition of the three modes with the equal magnitude  $\phi_\ell = \phi/2$

$$\phi_{\mathbf{r}} = \frac{\phi}{2} \sum_{\ell=1,2,3} \sigma_\ell \cos(\mathbf{Q}_\ell \cdot \mathbf{r}) v_\ell^+. \quad (\text{B9})$$

Note that  $\sigma_1\sigma_2\sigma_3$  in Eq. (B2) takes the value 1 in order to maximize the energy gain. The local order parameters are  $\phi_{\mathbf{r}} = \mathbf{0}$ ,  $\phi v_\ell^+$  ( $\ell = 1, 2, 3$ ) and this is a four-sublattice order with one disordered sublattice. For  $\sigma_1 = \sigma_2 = \sigma_3 = 1$ , the real space quadrupole moments form four-sublattice configuration with  $\phi_{(0,0)} = \mathbf{0}$ ,  $\phi_{(1,0)} = \hat{e}(\frac{\pi}{2})$ ,  $\phi_{(1/2, \sqrt{3}/2)} = \hat{e}(\frac{7\pi}{6})$ ,  $\phi_{(3/2, \sqrt{3}/2)} = \hat{e}(\frac{11\pi}{6})$ . See Fig. 1(c) in the main text. There are three other domains and they are realized by shifting the position  $\mathbf{r} \rightarrow \mathbf{r} - \frac{1}{2}(\sigma_1 + 2\sigma_2 + \sigma_3)\hat{e}(0) - \frac{1}{2}(2\sigma_1 + \sigma_2 + \sigma_3)\hat{e}(\omega/2)$ .

The total free energy density for the sTQ state is

$$\frac{F_{\text{sTQ}}}{N} = \frac{1}{2} \sum_{\ell=1,2,3} (a_0 + J_{\mathbf{Q}_\ell}^-) \left(\frac{\phi}{2}\right)^2 - \frac{3\lambda}{4}\phi^3 + \frac{3c}{4}\phi^4. \quad (\text{B10})$$

Here, we have used the relation  $\phi(\mathbf{Q}_\ell) = \sigma_\ell \phi v_\ell^+/2$ ,  $\mathbf{D} = \mathbf{0}$  when  $\phi_\ell = \phi/2$  and

$$J_{\mathbf{Q}_\ell}^- = -2J - 4K, \quad (K > 0). \quad (\text{B11})$$

The fact that one sublattice is disordered is apparent in the factor 3/4 of the fourth order term in Eq. (B10). In order to discuss the stability against the single- $\mathbf{q}$  order, it is useful to rescale  $\phi$  such that the quadratic term has the same form as in Eq. (B6):  $\phi = \frac{2}{\sqrt{3}}\varphi$ . The result is

$$\frac{F_{\text{sTQ}}}{N} = \frac{1}{2}(a_0 + J_{\mathbf{Q}}^-)\varphi^2 - \frac{2\lambda}{\sqrt{3}}\varphi^3 + \frac{4c}{3}\varphi^4. \quad (\text{B12})$$

The presence of  $\varphi^3$ -term demonstrates that the transition into the sTQ state is first order and its transition temperature is higher than that of the single- $\mathbf{q}$  state in the simple Landau analysis. This situation is similar to the cases in cubic systems<sup>49,50</sup>. However, as demonstrated in the main text, this is not the case when the fluctuation effects are taken account, and the transition becomes second order.

## 3. Asymmetric triple-q state for $K > 0$

The sTQ state is expected to be unstable at lower temperatures due to the presence of disordered sites. Here, we will

sketch the symmetry breaking from the sTQ to the asTQ states. Parameterizing  $\phi(\mathbf{0}) = \phi_0 \hat{e}(\theta_0)$  and  $\phi(\mathbf{Q}_\ell) = \Phi_\ell \hat{e}(\theta_\ell)$ , one finds that the cubic anisotropy energy in Eq. (B1) contains the following term

$$3\lambda \sum_{\ell=1}^3 \phi_0 \Phi_\ell^2 \sin(\theta_0 + 2\theta_\ell). \quad (\text{B13})$$

Let us consider small asymmetries in the three modes  $\Phi_\ell = \Phi + \delta_\ell$  and  $\theta_\ell = (1 - \frac{\ell}{4})\omega + \epsilon_\ell$ . Then, this term becomes

$$3\lambda \phi_0 \Phi \left\{ \sin \theta_0 \left[ -2\delta_1 + \delta_2 + \delta_3 - \sqrt{3}(\epsilon_2 - \epsilon_3) \Phi \right] + \cos \theta_0 \left[ \sqrt{3}(\delta_2 - \delta_3) + (-2\epsilon_1 + \epsilon_2 + \epsilon_3) \Phi \right] \right\}, \quad (\text{B14})$$

up to the linear order in  $\delta_\ell$  or  $\epsilon_\ell$ . This shows that the asymmetries in the three modes induce  $\phi(\mathbf{0})$ . Note that the  $\phi(\mathbf{0})$  is coupled with not only the magnitude asymmetry  $\delta_\ell$  but also the angle asymmetry  $\epsilon_\ell$ . This means that in general both the amplitude and the angle of  $\phi(\mathbf{Q}_\ell)$  in the asTQ state deviates from those in the sTQ state. Similar discussion has been done in Ref. 50.

## 4. Incommensurate triple-q state

Let us consider IC triple- $\mathbf{q}$  states. For simplicity, we restrict ourselves to the symmetric state for  $K > 0$ . Similarly to the case of the sTQ state,  $\phi_{\mathbf{r}}$  is expressed as

$$\phi_{\mathbf{r}} = \sum_{\ell=1,2,3} \frac{2\varphi}{\sqrt{6}} v_\ell^+ \cos(\mathbf{q}_\ell^* \cdot \mathbf{r} + \eta_\ell). \quad (\text{B15})$$

This corresponds to  $\phi(\mathbf{q}_\ell^*) = \sqrt{N/6} \varphi e^{i\eta_\ell} v_\ell^+$  and the free energy density reads as

$$\frac{F_{\text{IC-sTQ}}}{N} = \frac{1}{2}(a_0 + J_{\mathbf{q}^*}^-)\varphi^2 - \frac{2\lambda}{\sqrt{6}}\varphi^3 \cos \eta_{\text{tot}} + \frac{3c}{2}\varphi^4. \quad (\text{B16})$$

Here, in order to maximize the energy gain,  $\eta_{\text{tot}} = 2\pi \times (\text{integer})$  should be satisfied. Comparing this to Eq. (B12), one observes the commensurate locking, i.e., the third- and fourth-order terms have larger coefficients in Eq. (B16). See Sec. ??.

## 5. 120° antiferroic state

For  $K = 0$ , the ordering vectors locate at the K and K' points:  $\mathbf{q}_{\text{K}_1} = 2\omega \hat{e}_1$ ,  $\mathbf{q}_{\text{K}_2} = 2\omega \hat{e}_2$ ,  $\mathbf{q}_{\text{K}_3} = 2\omega \hat{e}_3$ , where the eigenvalues  $J_{\mathbf{q}_{\text{K}_\ell}}^\pm$  are degenerate. Thus, the directions of  $\phi(\mathbf{q}_{\text{K}_\ell})$  are not determined by the quadratic part of the free energy. The ordering configuration is chosen by the local third-order term which favors the three directions:  $\hat{e}(3\omega/4)$ ,  $\hat{e}(7\omega/4)$ , and  $\hat{e}(11\omega/4)$ . Such a 120° AF state is realized as a special case of the infinitely degenerate 120° structure. One realization is

$$\phi_{\mathbf{r}} = \frac{\phi}{\sqrt{2}} \left[ \frac{e^{i\mathbf{q}_{\text{K}_1} \cdot \mathbf{r}}}{\sqrt{2}} \begin{pmatrix} i \\ 1 \end{pmatrix} + \text{c.c.} \right] = \phi \begin{bmatrix} -\sin(\mathbf{q}_{\text{K}_1} \cdot \mathbf{r}) \\ \cos(\mathbf{q}_{\text{K}_1} \cdot \mathbf{r}) \end{bmatrix}. \quad (\text{B17})$$

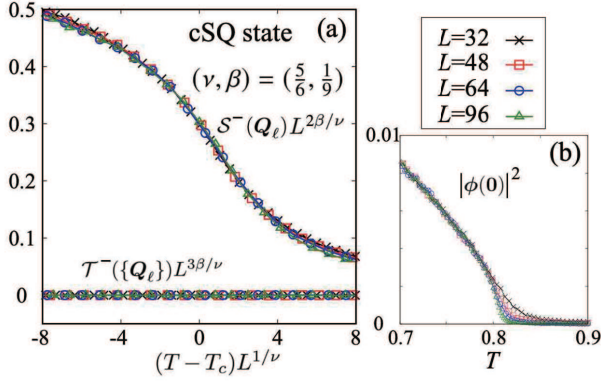


FIG. 5: (a) Finite-size scaling analysis of the order parameter structure factors for the transition to the cSQ state. The used exponents are those of the P3 universality class. The model parameters are  $\alpha = -3\pi/8$  and  $\lambda = 1$ , and the transition temperature is assumed  $T_c = 0.8032$ . Note that the eigenmode is  $v_\ell^-$  and the triple- $q$  structure factor  $\mathcal{T}^-$  vanishes. (b) The squared uniform moment  $|\phi(\mathbf{0})|^2$  vs  $T$ .

Since  $\phi(\mathbf{q}_{K_1}) = \sqrt{N}\phi/\sqrt{2}$ , the free energy is

$$\frac{F_{120^\circ}}{N} = \frac{1}{2}(a_0 - 3J)\phi^2 - \lambda\phi^3 + c\phi^4. \quad (\text{B18})$$

The presence of the  $\phi^3$ -term implies that the transition to a  $120^\circ$  AF state is first order. Indeed, the Monte Carlo data support this simple analysis.

## 6. Ferroic state

The ferroic quadrupolar state is simply given by  $\phi_r = \varphi v_\ell^+(\ell \in \{1, 2, 3\})$ . The direction of  $\phi_r$  is determined by the cubic term  $\lambda(> 0)$  and is three-fold degenerate. The free energy density is

$$\frac{F_F}{N} = \frac{1}{2}(a_0 + 6J)\varphi^2 - \lambda\varphi^3 + c\varphi^4. \quad (\text{B19})$$

Again, this predicts a first-order transition, but the results of our numerical simulation in the main text reveal it is second order.

## Appendix C: Monte Carlo simulation

In this Appendix, we will present several details of Monte Carlo (MC) data not shown in the main text. The exchange constants are parameterized as before as  $(J, K) = \bar{J}(\cos \alpha, \sin \alpha)$  with  $\bar{J} = 1$ .

### 1. Three-state Potts universality

Let us start to discuss the universality class of the transitions to the cSQ state. In contrast to the Ashkin-Teller class or the

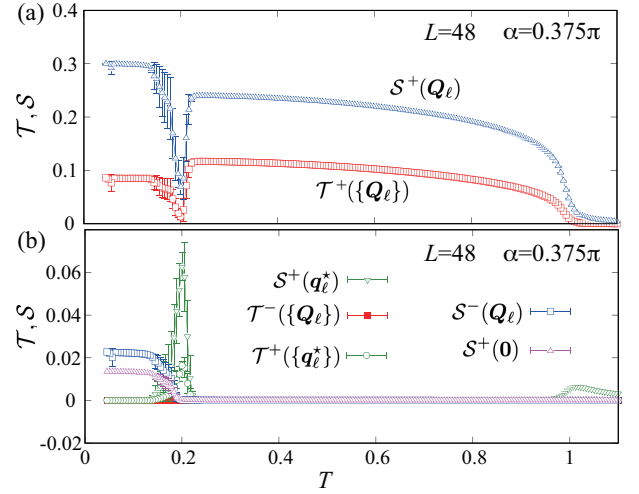


FIG. 6: Temperature dependence of various structure factors in the system with  $L = 48$ ,  $\alpha = 0.375\pi$ , and  $\lambda = 1$ . (a)  $S^+(\mathbf{Q}_\ell)$  and  $\mathcal{T}^+(\{\mathbf{Q}_\ell\})$  as a function of  $T$ . (b)  $S^+(\mathbf{q}_\ell^*)$ ,  $\mathcal{T}^-(\{\mathbf{Q}_\ell\})$ ,  $\mathcal{T}^+(\{\mathbf{q}_\ell^*\})$ ,  $S^-(\mathbf{Q}_\ell)$ , and  $S^+(\mathbf{0}) = S^-(\mathbf{0})$  as a function of  $T$ . Here,  $\mathbf{q}_\ell^* = \mathbf{Q}_\ell \pm \Delta_M \hat{e}_{4-\ell}$  with  $\Delta_M = \frac{4\pi}{3} \frac{1}{48}$ . Data are averaged over four ensembles that start from different initial configurations and are annealed for  $10^7$  MCS. Error bars show the standard deviation of these four sets.

four-state Potts (P4) of the sTQ order, it belongs to the three-state Potts (P3) class<sup>55</sup>. The transition to the F ordered state is also governed by the same P3 class, which we will not discuss here since this is a trivial one. As for the AF $120^\circ$  order, the transition is first order as expected in the six state Potts model in two dimensions<sup>55</sup>, and we will not discuss it furthermore.

Figure 5(a) shows the finite-size scaling analysis of the single- $q$  structure factor  $S^-(\mathbf{Q}_\ell)$  defined in the main text. The parameters are set to  $\alpha = -3\pi/8$  and  $\lambda = 1$ . For checking whether the triple- $q$  order is present, we have also calculated  $\mathcal{T}^-(\{\mathbf{Q}_\ell\})$ , but it turns out to be zero. This confirms the absence of triple- $q$  orders for  $K < 0$  and  $\lambda = 1$ . As clearly seen in Fig. 5(a), the data are well scaled with the exponents of the P3 class<sup>55</sup>. The cubic term  $\propto \lambda$  induces finite ferroic moments  $\phi(\mathbf{0})$ . Figure 5(b) shows the  $T$  dependence of the secondary order parameter  $|\phi(\mathbf{0})|^2$ . The size dependence is rather small below  $T_c = 0.8032$  and the data for different  $L$  collapse onto a single curve. This indicates  $|\phi(\mathbf{0})| > 0$  in the ordered state and this is what we have called the canted single- $q$  order: cSQ. The exponents for the secondary order parameter is also one of interesting recent topics<sup>77</sup> but here we do not discuss the detail.

### 2. Phase transition from sTQ to asTQ

We now discuss the symmetry breaking associated with the transition from the sTQ state to the asTQ state upon lowering  $T$ . This corresponds to the emergence of finite moments at the disordered sites in the sTQ state. Figures 6(a) and (b) show the  $T$ -dependence of the MC data of  $\mathcal{T}^+(\{\mathbf{Q}_\ell\})$ ,  $S^+(\mathbf{Q}_\ell)$ , and

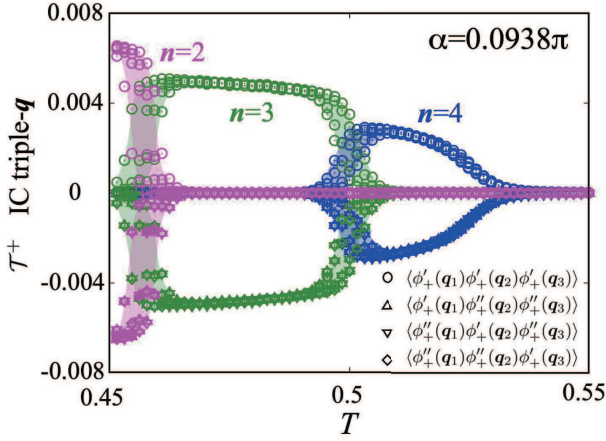


FIG. 7: Temperature dependence of the structure factor  $\mathcal{T}^+$  for  $\alpha = 0.0938\pi$ ,  $L = 50$ , and  $\lambda = 1$ .  $n$  represents the distance from the  $K'$  point:  $\mathbf{q}_\ell^* = \mathbf{q}_{K'} - \Delta_n \hat{e}_{4-\ell}$  ( $\Delta_n = \frac{4\pi n}{3L}$ ). The real part of  $\mathcal{T}^+$  consists of four parts and each of which contributes equally. The data with four different initial configurations with  $10^6$  MCS are shown and the shadows represent their approximate error bars as a guide to eyes.

$S^+(\mathbf{0})$  for  $\alpha = \frac{3\pi}{8}$ , which is the same parameter set used in Fig. 3(b) in the main text. For  $0.2 \lesssim T \lesssim 1$ , the sTQ state is realized, where both  $\mathcal{T}^+(\{\mathbf{Q}_\ell\})$  and  $S^+(\mathbf{Q}_\ell)$  are finite, while  $S^+(\mathbf{0}) = 0$ . As  $T$  decreases, the sTQ state is replaced by an IC triple- $\mathbf{q}$  state around  $T \approx 0.2$ . However, this IC state is unstable against the anisotropic triple- $\mathbf{q}$  state (asTQ) at the lower temperatures. This is seen in the fact that  $\mathcal{T}^+(\{\mathbf{Q}_\ell\})$  is smaller and  $S^+(\mathbf{Q}_\ell)$  is larger compared with those in the sTQ state. Note that the asTQ state has a nonvanishing  $S^\pm(\mathbf{0})$ . This is understood by noting that  $\mathbf{D}$  in Eq. (B3) is nonvanishing in the asTQ state. In addition to this, the structure factor for the non-dominant eigenmode  $S^-(\mathbf{Q}_\ell)$  is also finite, and this indicates that the moments  $\phi(\mathbf{r})$ 's rotate from the configuration in the sTQ state. See Fig. 6(b). Since the intermediate IC-TQ state appears only in a narrow region and this cannot be detected in small systems. Unfortunately, we could not simulate large enough systems to check the stability of the asTQ and IC-TQ states in this low temperature range. The ordering vectors  $\mathbf{q}^*$ 's are near the M points and the triple- $\mathbf{q}$  configuration and its moiré are slightly different from those discussed in the main text. We will briefly discuss this point at the end of Appendix C 3.

### 3. IC-triple- $\mathbf{q}$ state

In this section, we study IC triple- $\mathbf{q}$  states, focusing on the typical parameter set  $(J, K) = (\cos \alpha, \sin \alpha)$  with  $\alpha = 0.0938\pi$  used in the main text. See Fig. 3(c) in the main text.

First, let us analyze the detail of the triple- $\mathbf{q}$  structure factor  $\mathcal{T}^+(\{\mathbf{q}_\ell^*\})$ . As we have explained in the main text, it contains four terms as classified by the real ( $\phi'_+$ ) and imaginary ( $\phi''_+$ )

parts of the field  $\phi_+(\mathbf{q}_\ell)$

$$\begin{aligned} \mathcal{T}^+(\{\mathbf{q}_\ell^*\}) &= \langle \phi'_+(\mathbf{q}_1^*) \phi'_+(\mathbf{q}_2^*) \phi'_+(\mathbf{q}_3^*) \rangle \\ &\quad - [\langle \phi'_+(\mathbf{q}_1^*) \phi''_+(\mathbf{q}_2^*) \phi''_+(\mathbf{q}_3^*) \rangle + (\text{cyclic in } \mathbf{q}_\ell^*)]. \end{aligned} \quad (\text{C1})$$

Here,  $\langle \cdot \rangle$  denotes the MC average. Figure 7 shows  $T$ -dependence of these four terms for  $\alpha = 0.0938\pi$ ,  $L = 50$ , and  $\lambda = 1$ . The colors [magenta ( $n = 2$ ), green ( $n = 3$ ), blue ( $n = 4$ )] indicate the structure factor with different ordering vectors  $\mathbf{q}^* = \mathbf{q}_{K'} - \Delta_n \hat{e}_{4-\ell}$  with  $\Delta_n = \frac{4\pi n}{3L}$ . One can see the ordering vector gradually approach the  $K'$ (K) point as  $T$  decreases. Note that the data manifest the relation that the four terms in Eq. (C1) have an identical value,  $\langle \phi'_+(\mathbf{q}_1^*) \phi'_+(\mathbf{q}_2^*) \phi'_+(\mathbf{q}_3^*) \rangle = -\langle \phi'_+(\mathbf{q}_\ell^*) \phi''_+(\mathbf{q}_\ell^*) \phi''_+(\mathbf{q}_{\ell''}^*) \rangle$ , irrespective of the commensurability  $n$ . We can understand this relation by assuming that the phases  $\eta_\ell$  in the IC triple- $\mathbf{q}$  states are not locked but fluctuate over all the possible values. When  $\phi_\ell$ 's are all identical, one can set  $\phi'_+(\mathbf{q}_\ell^*) + i\phi''_+(\mathbf{q}_\ell^*) = \phi e^{i\eta_\ell}$  with  $\eta_{\text{tot}} = \eta_1 + \eta_2 + \eta_3 = 2\pi \times (\text{integer})$ . The constraint of the phase sum  $\eta_{\text{tot}}$  comes from the energy minimization in Eq. (B16). This leads to

$$\begin{aligned} \mathcal{T}^+(\{\mathbf{q}_\ell^*\}) &\propto \langle \cos \eta_1 \cos \eta_2 \cos \eta_3 \rangle \\ &\quad - [\langle \cos \eta_1 \sin \eta_2 \sin \eta_3 \rangle + (\text{cyclic in } \eta_\ell)]. \end{aligned} \quad (\text{C2})$$

It is easy to check that no set of fixed values of  $\eta_\ell$  satisfies the relation observed in our simulation. Instead, when integrating  $\eta_\ell$ 's under the assumption of uniform realization of all the possible values, we find

$$\int_{-\pi}^{\pi} \frac{d\eta_\ell}{2\pi} \int_{-\pi}^{\pi} \frac{d\eta_{\ell'}}{2\pi} \cos \eta_\ell \cos \eta_{\ell'} \cos(-\eta_\ell - \eta_{\ell'}) = \frac{1}{4}, \quad (\text{C3a})$$

$$\int_{-\pi}^{\pi} \frac{d\eta_\ell}{2\pi} \int_{-\pi}^{\pi} \frac{d\eta_{\ell'}}{2\pi} \cos \eta_\ell \sin \eta_{\ell'} \sin(-\eta_\ell - \eta_{\ell'}) = -\frac{1}{4}. \quad (\text{C3b})$$

This confirms no phase locking of the order parameters in the IC-TQ states.

Next, we visualize vortex configuration in our MC data. The sublattice vortex charge  $n_X(\mathbf{r})$  is defined in Eq. (6) in the main text and should be understood as a discrete sum along a closed path. We take  $\mathbf{r}$  in the sublattice X and consider the path formed by its nearest-neighbor X sites, i.e.,  $\mathbf{r}' \in X$ : hexagon vertices with their center at  $\mathbf{r}$ .

Figure 8 shows the short-time averaged snapshot of  $n_X(\mathbf{r})$  sampled over 1000 MCS. The parameters are  $\alpha = 0.0938\pi$ ,  $L = 50$ ,  $T = 0.489$ , and  $\lambda = 1$ . This is the configuration in the region of  $n = 3$  in Fig. 7. One can see an irregular honeycomb structure made of blue spots with  $n_X \sim -1/2$  and red spots at the center of each hexagon. The red spots have  $|n_X(\mathbf{r})| < 1$  but this is due to the short-time averaging. This confirms the formation of vortex lattice in the snapshot configurations of the IC-TQ state. The corresponding  $\phi(\mathbf{r})$  is shown in Fig. 3(c) in the main text and thus we do not discuss it here.

It is important to see what happens at the points where the ordering vector  $\mathbf{q}_\ell^*$  jumps in Fig. 7. Figures 9(a)–(c) show the order parameter angle  $\tilde{\theta}_r$  at  $T = 0.504$  in a larger system with  $L = 80$ . The other parameters are identical to those used in Fig. 7. This temperature is the point where  $n$  changes from 6

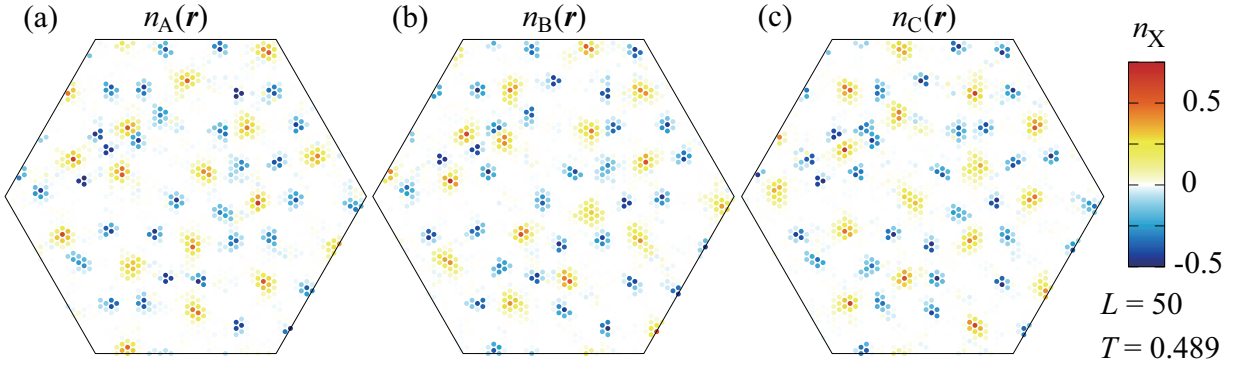


FIG. 8: Snapshots of sublattice vortex charge configurations at  $T = 0.489$ . The data are averaged over 1000 MCS for  $L = 50$ ,  $\alpha = 0.0938\pi$ , and  $\lambda = 1$ .

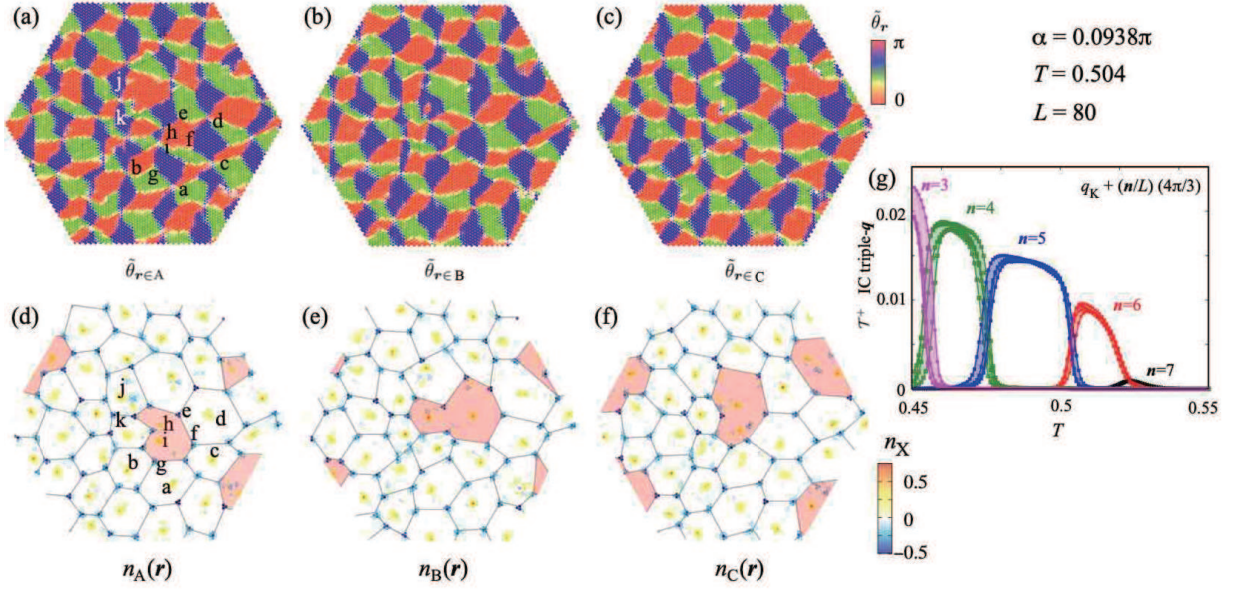


FIG. 9: Snapshots of the order parameter angles  $\tilde{\theta}_r$  in (a)-(c) and vortex charges  $n_X(\mathbf{r})$  in (d)-(f) at  $T = 0.504$  in the system with  $\alpha = 0.0938\pi$ ,  $L = 80$ , and  $\lambda = 1$ . The data are averaged over 1000 MCS. In (d)-(f), the vortices are connected by lines for guide to the eye, and dislocation positions are indicated by red shade. In (a) and (d), several vortices are labeled by letters a–k. (g) Temperature dependence of the IC-TQ structure factor  $\mathcal{T}^+$ . Except  $T$ , all the parameters are identical to those for (a)-(f). These are calculated for four ensembles annealed for  $10^6$  MCS starting from different initial configurations. Their statistical errors are shown by shadows as guide to the eye. The data in (a)-(f) corresponds to the boundary between the  $n = 5$  and 6 parts.

to 5 inside the IC-TQ state. As shown in Fig. 9(g),  $n$  varies as  $T$  decreases. See similar behavior for  $L = 50$  in Fig. 7. In Fig. 9(a), some vortex cores are labeled by letters. Let us focus on the islands with green color. They align along a set of lines running slightly up diagonally to the left. One can see a dislocation at the position h, and a new line of green islands starts from there. A dislocation also exists in the panels (b) and (c) at the same position in the vortex lattices.

To visualize dislocations more clearly, we have calculated the vortex charge distribution and show the results in Figs. 9(d)–(f). Blue spots are vortex cores and we have connected them by gray lines to visualize a honeycomb-like structure of their arrangement. The non-hexagon areas in light red are the regions including dislocations. It is well-known that

such dislocation formation in two-dimensions indeed destroys long-range order of crystal<sup>60</sup>. Thus, a two-dimensional “crystal” acquires only a quasi-long-range order via the Kosterlitz-Thouless (KT) transition at  $T = T^*$ <sup>24</sup>. In the theory of the commensurate-IC transition, it was predicted that even a KT transition does not occur and the system remains a liquid in some situations<sup>61</sup>. In our MC simulations, it is hard to check whether this phase is critical or not by examining the vortex degrees of freedom such as the vortex charge correlation function. This is because the maximum system size  $L \sim 100$  is still too small in the sense that the number of vortices is not sufficient to study whether they form a crystal or remain disordered.

In contrast, orbital degrees of freedom  $\phi$  exhibit a trace of

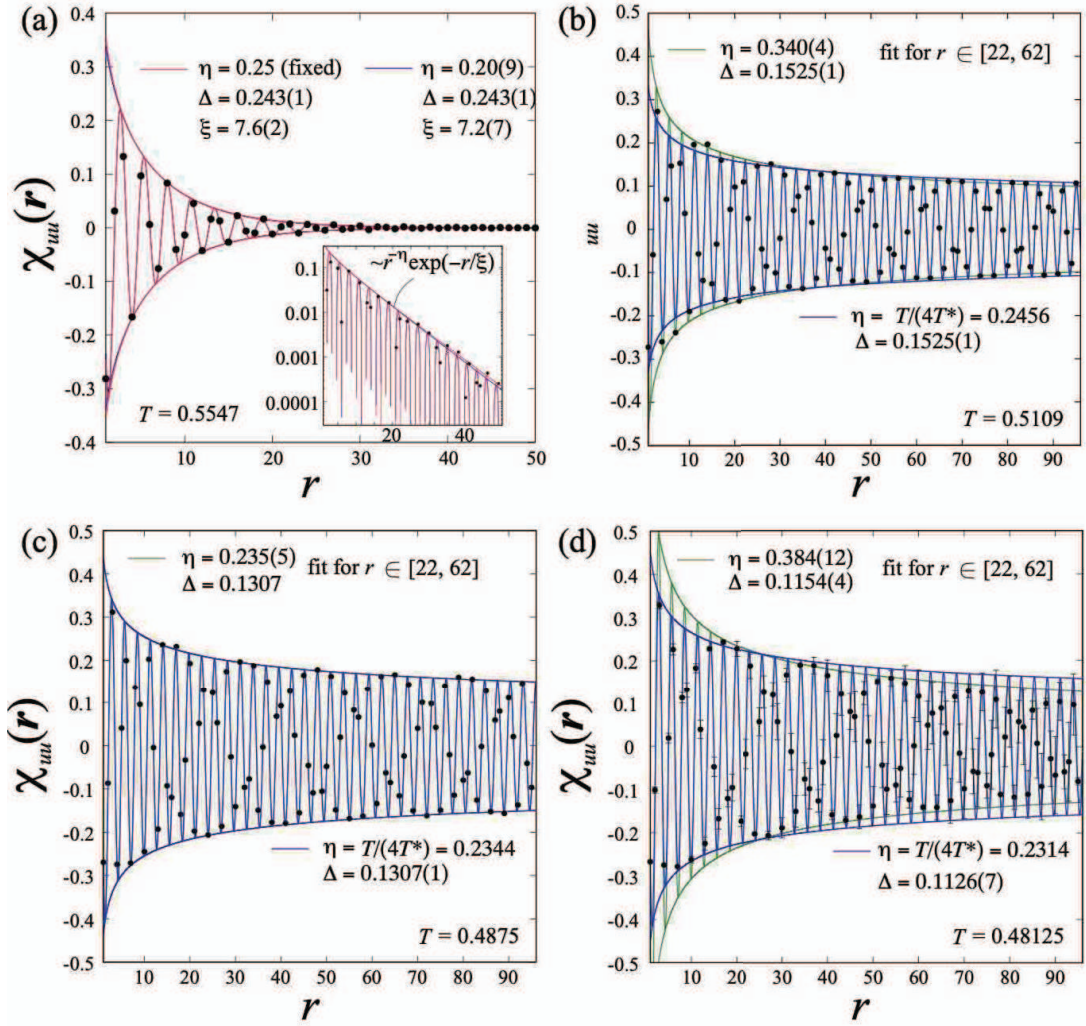


FIG. 10: Real-space correlation function  $\chi_{uu}(\mathbf{r})$  for  $\mathbf{r} = r\hat{e}_0$  in the system with  $L = 96$ . The data for  $r$  along equivalent directions are averaged to reduce statistical errors.  $T$  is (a) 0.5547, (b) 0.5109, (c) 0.4875, and (d) 0.48125, while  $T^* \simeq 0.518$ . Filled circles are the Monte Carlo data with averaging over eight sets of  $3 \times 10^6$  MCS. Lines in the panels are  $\sim e^{-r/\xi} \cos[(\Delta/2 + 2\pi/3)r]r^{-\eta}$  in (a) and  $\sim \cos[(\Delta/2 + 2\pi/3)r]r^{-\eta}$  in (b)-(d), and the parameter values are shown in each panel. Inset in (a) is a semilogarithmic plot.

quasi-long-range order. We consider their fluctuations in the thermodynamic limit are not qualitatively influenced by the variation of IC ordering vector  $\mathbf{q}^*$ . The vector  $\mathbf{q}^*$  is expected to change smoothly without discrete jumps and the correlation functions of  $\phi$  exhibit quasi-long-range behavior similar to the KT phase in the XY model<sup>24</sup>. However, it is not easy to analyze the exponent in the correlation functions, since the change of  $\mathbf{q}^*$  remains discontinuous with lowering  $T$  in finite size systems. This makes it difficult to find the behavior in the thermodynamic limit based on finite-size simulations. Nevertheless, as will be explained below, our results show the existence of the KT behavior in the orbital  $\phi$  sector.

Let us discuss the real-space correlation function in the IC-TQ state for  $K > 0$ ,

$$\chi_{ij}(\mathbf{r}) \equiv \langle \phi_{i,\mathbf{r}} \phi_{j,0} \rangle, \quad (i, j \in \{u, v\}). \quad (\text{C4})$$

To simplify the following discussion, we concentrate on  $\chi_{uu}(\mathbf{r})$  for  $\mathbf{r} = (r, 0)$  with  $r$  being an integer.

The actual Monte Carlo data of  $\chi_{uu}(\mathbf{r})$  are well fitted by power-law dependence on  $r$  with a oscillation factor as

$$\chi_{uu}(\mathbf{r}) \propto \frac{1}{r^\eta} \cos \left[ \left( \frac{2\pi}{3} + \frac{\Delta}{2} \right) r \right] \quad \text{for } T < T^*. \quad (\text{C5})$$

For  $T > T^*$ , Eq. (C5) is easily extended to that by including the multiplication factor  $\exp(-r/\xi)$  with  $\xi$  being the correlation length.

Figure 10 shows the Monte Carlo data of  $\chi_{uu}(\mathbf{r})$ , and the result of their fitting with Eq. (C5). One should note that the panel (d) shows the result for the parameter set near the phase boundary to another phase with different  $\mathbf{q}^*$ . Except for this, the fitting works well with the expression (C5) in (b) and (c), and with the corresponding expression for  $T > T^*$  in (a). For

comparison, the fitting with  $\eta_{\text{KT}} = T/(4T^*)$  ( $T^* \simeq 0.518$ ), expected in the simple scaling analysis of the KT transition, is also shown with green curves in (b)–(d) for  $T < T^*$  together with those obtained via fitting for  $22 \leq r \leq 62$ . In (c), the  $\eta$  value is almost identical to the expected value  $\eta_{\text{KT}}$ , while larger in (b). The latter is due to the fact that the phase with  $n = 8$  is narrow and the structure factors  $\mathcal{S}^+(\mathbf{q}_\ell^*)$  and  $\mathcal{T}^+(\{\mathbf{q}_\ell^*\})$  are much smaller than those in the other low- $T$  phases. Nevertheless, the difference between the green and blue curves is rather small in (b) for the intermediate distance regime  $30 \lesssim r \lesssim 70$ , where the short-range correlation and the effects of the periodic boundary are both small. For lower  $T$ , whether the simple form  $\eta_{\text{KT}}(T)$  is valid or not is nontrivial, and the quantitative discussion well below  $T^*$  needs more elaborate and careful analysis. Recently, such analysis has been done in a frustrated transverse-field Ising model<sup>77</sup>, where their numerical data show  $\eta \sim \eta_{\text{KT}}$  even for low  $T$  regime in the expected KT phase.

Figure 11(a) shows  $\eta(T)$  determined by fitting the Monte Carlo data for  $L = 96$ . In the fitting, several choices of fitting region have been examined. As we have mentioned, the results show noticeable deviation from  $\eta_{\text{KT}}(T)$  (green line) around  $T^* \simeq 0.518$  and near the boundaries between phases with different  $\mathbf{q}^*$ 's. For the temperatures well inside each phase, the data sets plotted in blue are close to  $\eta_{\text{KT}}$ , and they are fitted for  $20 \leq r \leq 70$  inside the  $n = 6$  and 7 phases. Even above  $T^*$ , the data can be fitted by Eq. (C5) if  $\xi > L$ , but this is an artifact of finite system size. For lower  $T$ , we expect that the  $\mathbf{q}^*$  vector further moves toward the K point, but we could not carry out efficient numerical simulations at the lower temperatures.

The correlation function of  $\phi(\mathbf{q})$  also exhibits an evidence of the quasi-long-range order. Figure 11(b) shows the  $T$  dependence of the exponent  $\zeta$  for  $L = 96$  in  $\mathcal{S}^+(\mathbf{q}) \simeq |\delta\mathbf{q}|^{-\zeta}$  with  $\delta\mathbf{q} \equiv \mathbf{q} - \mathbf{q}_\ell^*$  for several fitting ranges. To reduce the effects of subleading hexagonal anisotropy, the two data sets along  $\delta\mathbf{q} \parallel \hat{e}(\ell\omega)$  and  $\parallel \hat{e}((\ell - \frac{1}{4})\omega)$  are averaged.  $\mathcal{S}^+(\mathbf{q})$  has six peaks in the 1BZ. Its dependence of a specific  $\mathbf{q} - \mathbf{q}_\ell^*$  is affected by the other peaks at  $\mathbf{q}_{\ell' \neq \ell}^*$ . Since this is noticeable at  $|\delta\mathbf{q}| \sim 0.4$ , we choose the fitting ranges  $0.5 \leq |\delta\mathbf{q}| \leq 2.5$  and  $0.01 \leq |\delta\mathbf{q}| \leq 0.3$ . We observe that the data obtained by the shorter-range fit in  $\delta\mathbf{q}$  follow  $\eta_{\text{KT}}$  dependence (sky-blue triangle), and that all the four fitting schemes show increasing  $\zeta$  with lowering  $T$ , when ignoring the behavior near the phase boundaries between the different  $n$ 's.

Overall, the results shown in Fig. 11 are qualitatively consistent with the scenario that the KT transition occurs and the IC-TQ state possesses a quasi-long-range order. To quantitatively estimate the exponents and carry out calculations at lower temperatures, more elaborate numerical simulations are necessary.

To close this section, let us show a typical moiré texture and choose  $\mathbf{q}_\ell^* \simeq \mathbf{Q}_\ell - \frac{\pi}{8}\hat{e}_{4-\ell}$ . Figure 12(a) shows  $\phi(\mathbf{r})$  calculated by the superposition of the triple- $\mathbf{q}$  plane waves, which is not the results of MC simulations. The cubic potential energy  $\sin 3\theta_r$  is also shown in Fig. 12(b), which exhibits a ‘‘charge’’ moiré pattern. Note also that  $\sin 3\theta_r < 0$  at the most of the sites. Similarly to the case discussed in the main text, one defines the vortex charge  $n_X(\mathbf{r})$  for the four sublattices

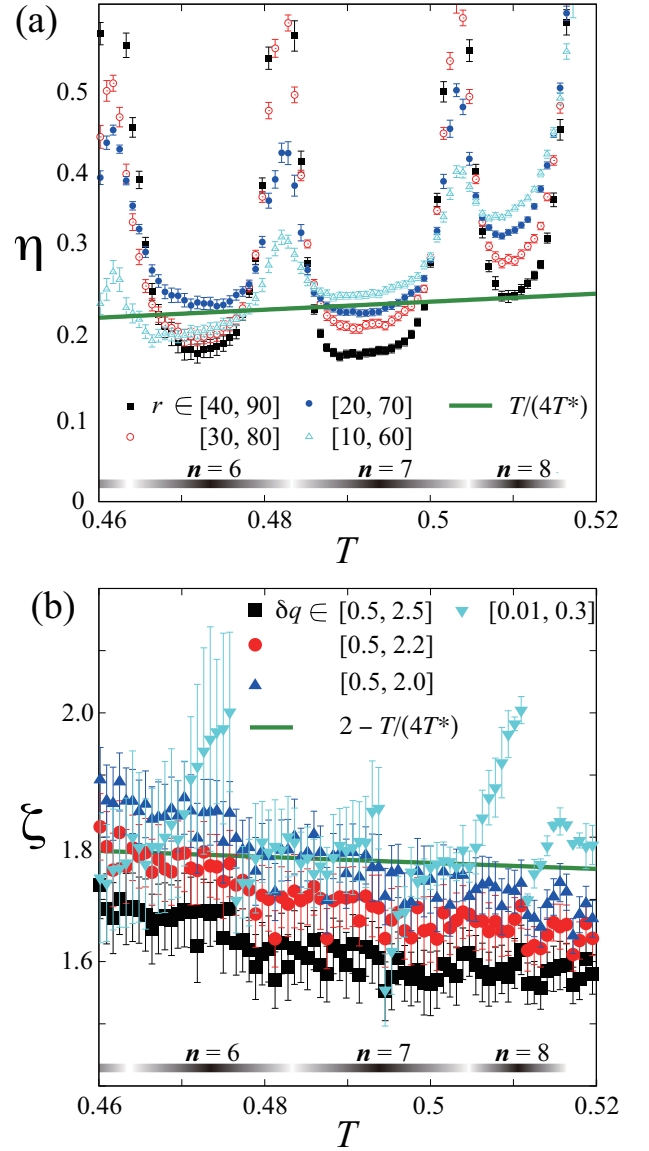


FIG. 11: Temperature dependence of estimated exponents  $\eta$  and  $\zeta$  for the system with  $L = 96$ . They define critical behaviors of the correlation functions as  $\chi_{uu}(\mathbf{r}) \sim r^{-\eta}$  and  $\mathcal{S}^+(\mathbf{q}) \sim |\delta\mathbf{q}|^{-\zeta}$  below  $T^* = 0.518$ . The four sets correspond to different fitting ranges  $r \in [r_0, r_1]$  in (a) and  $\delta\mathbf{q} \equiv |\mathbf{q} - \mathbf{q}^*| \in [q_0, q_1]$  in (b). Green lines indicate  $\eta_{\text{KT}} = \frac{1}{4}(T/T^*)$  and  $\zeta_{\text{KT}} = 2 - \frac{1}{4}(T/T^*)$  expected for the KT phase. The parameter  $n$  is a parameter for  $\Delta_n$  and specifies the  $\mathbf{q}^*$  vector position. The peak structure near the boundaries between two regions with different  $n$ 's is due to the presence of two different modulations in the system.

( $X=A,B,C,D$ ) and the result for  $X = A$  is shown in Fig. 12(c). This texture is similar to that in Fig.2(b) in the main text. In our simulation, this type of moiré pattern is indeed fragile and only observed in a narrow regime between the sTQ and asTQ states. This might be related to the strong stability of the sTQ state. Thus, for stabilizing this type of moiré pattern, an

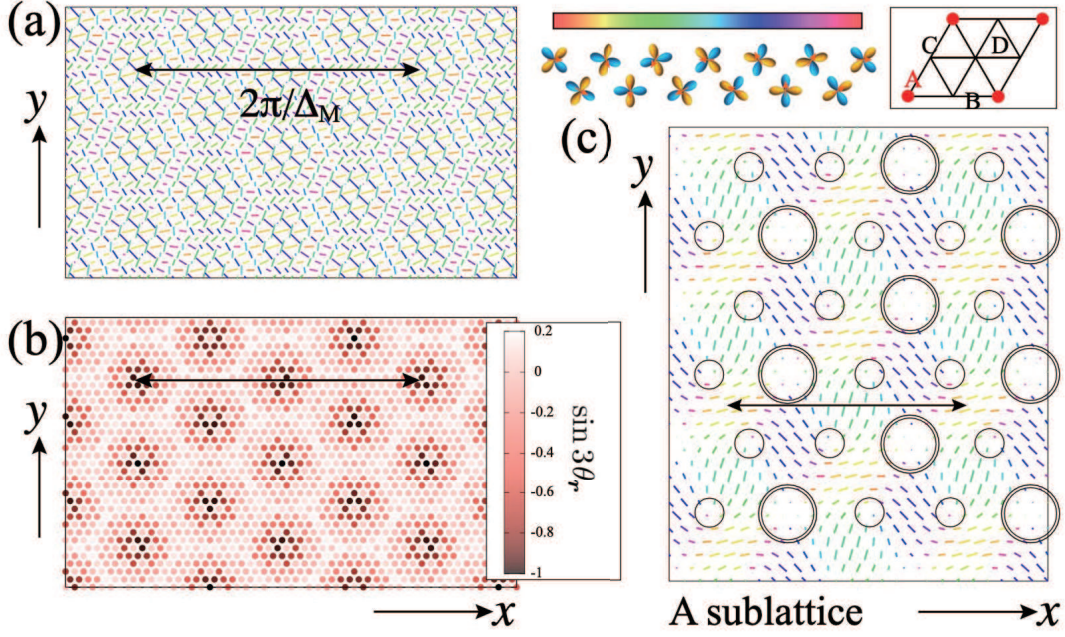


FIG. 12: Several configurations in the triple- $q$  state with  $q_\ell^* = Q_\ell - \Delta_M \hat{e}_{4-\ell}$  with  $\Delta_M = \frac{\pi}{8}$ . Direction of each local orbital/director is shown by color in the chart at the right top. Sublattice labels are also shown there. (a) The director angle  $\tilde{\theta}_r$ . The length of each bar represents  $|\phi(r)|$ . (b) The color plot of the potential  $\sin 3\theta_r$ . (c) The A-sublattice structure of (a). Vortices and half-vortices are shown by double-line big circles and single-line small circles, respectively. The periodicity of the configuration is shown by a double-headed arrow in each panel.

alternative model is necessary.

#### Appendix D: $D_6$ point group

In the last part in the main text, we pointed out the possible patterns of induced polarization and current induced magnetization. Here, we sketch their group theoretical analysis when the local symmetry is the point group  $D_6$ . Let us summarize the irreducible representations made from the two-component quadrupole moments  $\phi = (\phi_u, \phi_v)$ , the magnetic moments  $M = (M_x, M_y, M_z) =: (M_\perp, M_z)$ , and the electric currents  $j = (j_x, j_y, j_z) =: (j_\perp, j_z)$ . The character table of the  $D_6$  group is shown in Table I. It is noted that the basis sets of the  $E_1$  irrep are the planer magnetic moment  $M_\perp$ , position (or polarization)  $(x, y)$ ,  $\nabla_\perp \equiv (\partial_x, \partial_y)$ , and planer current  $j_\perp$ , while  $\phi$  is the  $E_2$  irrep. The remaining  $j_z$ ,  $M_z$ , and  $z$  belong to the  $A_2$  irrep.

We list below the decomposition of the direct products including  $j$ .

- $A_1$ :  $j_z M_z, j_\perp \cdot M_\perp$ ,
- $A_2$ :  $j_x M_y - j_y M_x =: j_\perp \times M_\perp$ ,
- $E_1$ :  $j_\perp M_z, j_z M_\perp$ ,
- $E_2$ :  $(j_x M_y + j_y M_x, j_x M_x - j_y M_y)$ .

For the terms including  $\nabla \otimes \phi = E_1 \otimes E_2 \oplus A_2 \otimes E_2$ ,

TABLE I: The character table of the  $D_6$  point group.

irrep	$E$	$2C_6$	$2C_3$	$C_2$	$3C_{2y}$	$3C_{2x}$	basis
$A_1, \Gamma_1$	1	1	1	1	1	1	$z^2$
$A_2, \Gamma_2$	1	1	1	1	-1	-1	$z, M_z$
$B_1, \Gamma_3$	1	-1	1	-1	1	-1	$y^3 - 3x^2y$
$B_2, \Gamma_4$	1	-1	1	-1	-1	1	$x^3 - 3xy^2$
$E_1, \Gamma_6$	2	1	-1	-2	0	0	$\{x, y\}, \{M_x, M_y\}$
$E_2, \Gamma_5$	2	-1	-1	2	0	0	$\{2xy, x^2 - y^2\}$

- $B_1$ :  $\nabla_\perp \cdot \phi = \partial_x \phi_u + \partial_y \phi_v$ ,
- $B_2$ :  $\partial_x \phi_v - \partial_y \phi_u =: \nabla_\perp \times \phi$ ,
- $E_1$ :  $(\partial_x \phi_v + \partial_y \phi_u, \partial_x \phi_u - \partial_y \phi_v) =: \pi_\perp = (\pi_x, \pi_y)$ ,
- $E_2$ :  $\partial_z \phi = (\partial_z \phi_u, \partial_z \phi_v)$ .

Now, we consider the quadrupole pattern that transforms in the same way as polarization. That is  $\pi_\perp$  belonging to the  $E_1$  irrep. Its contribution to energy under finite  $j$  is nothing but the invariants including both  $\pi_\perp$  and  $j$ . They are easily constructed by multiplying its  $E_1$  counterpart including  $j$ . There are two invariants:  $M_z(\pi_\perp \times j_\perp)$  and  $(M_\perp \times \pi_\perp)j_z$ . Introducing the three component representation  $\pi \equiv (\pi_\perp, 0)$ , they read  $M_z(\pi \times j)_z$  and  $(M \times \pi)_z j_z$  as discussed in the main text.

### Appendix E: Commensurate “locking”

As we have discussed in the main text, the IC-TQ state appears for  $K > 0$  between the AF  $120^\circ$  and the sTQ states. The ordering vectors  $\mathbf{q}^*$  vary as functions of  $T$  and also the interaction parameter  $\alpha$ . One of the origins of these variations is that the minimum of the exchange coupling  $J_{\mathbf{q}^*}^-$  is shallow as shown in Fig. 4(b). Thus, the energy gain of the quadratic term in the free energy is small and the fourth-order terms become important. In Eqs. (B6), (B8), (B12), (B16), (B18), and (B19), one can see the forth-order terms prefer commensurate orders, which manifests commensurate locking. Here, we summarize a simple argument about the commensurate locking with taking account of higher order terms in the Landau free energy. Consider a real scalar field  $\psi(x)$  defined in the one-dimensional lattice with length  $L$  (lattice constant 1) under the periodic boundary condition. In this case,  $q$  is quantized as  $q = 2\pi n/L$  with  $n \in \{-L/2 + 1, \dots, 0, 1, \dots, L/2\}$ .

In order to understand the difference between the “general”  $q$  points and the “high-symmetric”  $q$  points, we consider local energy  $E_2$  and  $E_4$ :

$$E_2 = \sum_{j=0}^{L-1} \psi^2(x_j), \quad \text{and} \quad E_4 = \sum_{j=0}^{L-1} \psi^4(x_j). \quad (\text{E1})$$

Let us consider a simple configuration  $\psi(x_j) = \cos(qj)$  and examine the corresponding energies. We obtain

$$E_2 = \frac{1}{2} \sum_j [1 + \cos(2qj)] = \begin{cases} L & \text{for } q = 0 \text{ and } \pi \\ \frac{1}{2}L & \text{for the other } q\text{'s} \end{cases}. \quad (\text{E2a})$$

$$E_4 = \frac{1}{8} \sum_j [3 + 4 \cos(2qj) + \cos(4qj)] = \begin{cases} L & \text{for } q = 0 \text{ and } \pi \\ \frac{1}{2}L & \text{for } q = \pm\pi/2 \\ \frac{3}{8}L & \text{for the other } q\text{'s} \end{cases}. \quad (\text{E2b})$$

From these expressions, one can find a clear contrast between the general  $q$  points and the high-symmetry  $q$  points.

Alternatively, we can derive the same results by calculations in  $q$ -space sum. Let  $c_q$  denote the Fourier component of  $\psi(x)$ . The reality imposes the relation  $c_{-q} = c_q^*$ . First,  $E_2$  reads

$$E_2 = \sum_q |c_q|^2 = c_0^2 + c_\pi^2 + 2 \sum_{0 < q < \pi} |c_q|^2. \quad (\text{E3})$$

Note that  $c_0$  and  $c_\pi$  are both real and the general- $q$  terms appear twice in the form of  $c_q c_{-q}$  and  $c_{-q} c_q$ , while  $q = 0$  and  $\pi$  appear once. These results completely agree with Eq. (E2a) by substituting  $c_0 = \sqrt{L}$ ,  $c_\pi = \sqrt{L}$ , or  $c_q = \sqrt{L}/2$  for  $0 < q < \pi$ . Next consider  $E_4$ ,

$$E_4 = \frac{1}{L} \sum_{qq'pp'} \sum_G c_q c_{q'} c_p c_{p'} \delta_{q+q'+p+p', G} = \frac{1}{L} \left[ c_0^4 + c_\pi^4 + 6\text{Re}(c_{\pi/2}^4) + 6 \sum_{0 < q < \pi} |c_q|^4 + \dots \right], \quad (\text{E4})$$

where  $\{G = 2\pi \times (\text{integer})\}$  are the reciprocal lattice vectors. Note  $\text{Re}(c_{\pi/2}^4) = \text{Re}(c_{-\pi/2}^4)$ , and we have written down only terms relevant for the discussion about the single- $q$  orders. The factor 6 arises from the combinatorial number choosing two  $c_q$ 's out of four.  $c_{\pi/2}^4$  and  $c_\pi^4$  terms arise from the Umklapp conditions with  $G = \pm 2\pi$  and  $G = \pm 4\pi$ , respectively. Again, substituting  $c_0 = c_\pi = \sqrt{L}$  and  $c_{\pm q} = \sqrt{L}/2$  for  $0 < q < \pi$ , the results reproduce Eq. (E2b). These results demonstrate that the free energy has different coefficients between the general- $q$  and high-symmetry- $q$ , and this reflects the tendency of “locking” of the ordering vectors to the rational (high-symmetry) ones.

\* hattori@tmu.ac.jp

<sup>1</sup> I. Amidror, The Theory of the Moiré Phenomenon, Vol. I: Periodic Layers (Springer Science & Business Media (London), 2009).  
<sup>2</sup> Y. Xiao, J. Liu, and L. Fu, *Matter* **3**, 1142 (2020).  
<sup>3</sup> D. M. Kennes, M. Claassen, L. Xian, A. Georges, A. J. Millis, J. Hone, C. R. Dean, D. N. Basov, A. N. Pasupathy, and A. Rubio, *Nat. Phys.* **17**, 155 (2021).  
<sup>4</sup> M. Yankowitz, S. Chen, H. Polshyn, Y. Zhang, K. Watanabe, T. Taniguchi, D. Graf, A. F. Young, and C. R. Dean, *Science* **363**, 1059 (2019).  
<sup>5</sup> G. Chen, A. L. Sharpe, P. Gallagher, I. T. Rosen, E. J. Fox, L. Jiang, B. Lyu, H. Li, K. Watanabe, T. Taniguchi, J. Jung, Z. Shi, D. Goldhaber-Gordon, Y. Zhang, and F. Wang, *Nature* **572**, 215 (2019).  
<sup>6</sup> W. Wang, G. Zhou, W. Lin, Z. Feng, Y. Wang, M. Liang, Z. Zhang, M. Wu, L. Liu, K. Watanabe, T. Taniguchi, W. Yang, G. Zhang, K. Liu, J. Gao, Y. Liu, X. C. Xie, Z. Song, and X. Lu, *Phys. Rev. Lett.* **132**, 246501 (2024).

<sup>7</sup> H. Li, J. Wu, Z. Yin, and H. Zhang, *Acc. Chem. Res.* **47**, 1067 (2014).  
<sup>8</sup> K. Hippalgaonkar, Y. Wang, Y. Ye, D. Y. Qiu, H. Zhu, Y. Wang, J. Moore, S. G. Louie, and X. Zhang, *Phys. Rev. B* **95**, 115407 (2017).  
<sup>9</sup> M.-L. Lin, Q.-H. Tan, J.-B. Wu, X.-S. Chen, J.-H. Wang, Y.-H. Pan, X. Zhang, X. Cong, J. Zhang, W. Ji, P.-A. Hu, K.-H. Liu, and P.-H. Tan, *ACS Nano* **12**, 8770 (2018).  
<sup>10</sup> J.-X. Lin, P. Siriviboon, H. D. Scammell, S. Liu, D. Rhodes, K. Watanabe, T. Taniguchi, J. Hone, M. S. Scheurer, and J. I. A. Li, *Nat. Phys.* **18**, 1221 (2022).  
<sup>11</sup> M. M. Al Ezzi, J. Hu, A. Ariando, F. Guinea, and S. Adam, *Phys. Rev. Lett.* **132**, 126401 (2024).  
<sup>12</sup> W.-Y. He, D. Goldhaber-Gordon, and K. T. Law, *Nat. Commun.* **11**, 1650 (2020).  
<sup>13</sup> B. Xie, R. Peng, S. Zhang, and J. Liu, *NPJ Comput. Mater.* **8**, 1 (2022).  
<sup>14</sup> V. P. Mineev, *Low Temp. Phys.* **39**, 818 (2013).

- 15 D. A. Ivanov, Phys. Rev. Lett. **86**, 268 (2001).
- 16 J. Garaud and E. Babaev, Phys. Rev. B **86**, 060514(R) (2012).
- 17 A. A. Zyuzin, J. Garaud, and E. Babaev, Phys. Rev. Lett. **119**, 167001 (2017).
- 18 J. R. Abo-Shaer, C. Raman, J. M. Vogels, and W. Ketterle, Science **292**, 476 (2001).
- 19 H. Takeuchi, Phys. Rev. Lett. **126**, 195302 (2021).
- 20 L. Chen, Y. Zhang, and H. Pu, Phys. Rev. Lett. **125**, 195303 (2020).
- 21 Y. G. Rubo, Phys. Rev. Lett. **99**, 106401 (2007).
- 22 K. G. Lagoudakis, T. Ostatnický, A. V. Kavokin, Y. G. Rubo, R. André, and B. Deveaud-Plédran, Science **326**, 974 (2009).
- 23 H. Flayac, I. A. Shelykh, D. D. Solnyshkov, and G. Malpuech, Phys. Rev. B **81**, 045318 (2010).
- 24 J. M. Kosterlitz and D. J. Thouless, J. Phys. C **6**, 11811 (1973).
- 25 U. K. Rössler, A. N. Bogdanov, and C. Pfeleiderer, Nature **442**, 797 (2006).
- 26 S. Mühlbauer, B. Binz, F. Jonietz, C. Pfeleiderer, A. Rosch, A. Neubauer, R. Georgii, and P. Böni, Science **323**, 915 (2009).
- 27 A. Tonomura, X. Yu, K. Yanagisawa, T. Matsuda, Y. Onose, N. Kanazawa, H. S. Park, and Y. Tokura, Nano Lett. **12**, 1673 (2012).
- 28 Y. Tokura and N. Kanazawa, Chem. Rev. **121**, 2857 (2021).
- 29 K. Shimizu, S. Okumura, Y. Kato, and Y. Motome, Phys. Rev. B **103**, 184421 (2021).
- 30 K. Shimizu, S. Okumura, Y. Kato, and Y. Motome, J. Phys. Conf. Ser. **2164**, 012069 (2022).
- 31 N. Kanazawa, J.-H. Kim, D. S. Inosov, J. S. White, N. Egetenmeyer, J. L. Gavilano, S. Ishiwata, Y. Onose, T. Arima, B. Keimer, and Y. Tokura, Phys. Rev. B **86**, 134425 (2012).
- 32 S. Ishiwata, T. Nakajima, J.-H. Kim, D. S. Inosov, N. Kanazawa, J. S. White, J. L. Gavilano, R. Georgii, K. M. Seemann, G. Brandl, P. Manuel, D. D. Khalyavin, S. Seki, Y. Tokunaga, M. Kinoshita, Y. W. Long, Y. Kaneko, Y. Taguchi, T. Arima, B. Keimer, and Y. Tokura, Phys. Rev. B **101**, 134406 (2020).
- 33 B. Göbel, I. Mertig, and O. A. Tretiakov, Phys. Rep. **895**, 1 (2021).
- 34 A. Fert, M. Chshiev, A. Thiaville, and H. Yang, J. Phys. Soc. Jpn. **92**, 081001 (2023).
- 35 T. Okubo, S. Chung, and H. Kawamura, Phys. Rev. Lett. **108**, 017206 (2012).
- 36 Y. Akagi, M. Udagawa, and Y. Motome, Phys. Rev. Lett. **108**, 096401 (2012).
- 37 S. Hayami and Y. Motome, J. Phys.: Cond. Matt. **33**, 443001 (2021).
- 38 Z. Wang, Y. Su, S.-Z. Lin, and C. D. Batista, Phys. Rev. B **103**, 104408 (2021).
- 39 R. Yambe and S. Hayami, Phys. Rev. B **106**, 174437 (2022).
- 40 R. Yambe and S. Hayami, Phys. Rev. B **107**, 174408 (2023).
- 41 M. Hirschberger, S. Hayami, and Y. Tokura, New J. Phys. **23**, 023039 (2021).
- 42 B. R. Ortiz, L. C. Gomes, J. R. Morey, M. Winiarski, M. Bordelon, J. S. Mangum, I. W. H. Oswald, J. A. Rodriguez-Rivera, J. R. Neilson, S. D. Wilson, E. Ertekin, T. M. McQueen, and E. S. Toberer, Phys. Rev. Mat. **3**, 094407 (2019).
- 43 M. M. Denner, R. Thomale, and T. Neupert, Phys. Rev. Lett. **127**, 217601 (2021).
- 44 T. Ishitobi and K. Hattori, Phys. Rev. B **104**, L241110 (2021).
- 45 T. Yanagisawa, H. Matsumori, H. Saito, H. Hidaka, H. Amitsuka, S. Nakamura, S. Awaji, D. I. Gorbunov, S. Zherlitsyn, J. Wosnitza, K. Uhlířová, M. Vališka, and V. Sechovský, Phys. Rev. Lett. **126**, 157201 (2021).
- 46 T. Ishitobi and K. Hattori, Phys. Rev. B **107**, 104413 (2023).
- 47 M. B. Walker, C. Kappler, K. A. McEwen, U. Steigenberger, and K. N. Clausen, J. Phys.: Cond. Matt. **6**, 7365 (1994).
- 48 A. V. Nikolaev and K. H. Michel, Euro. Phys. J. B **9**, 619 (1999).
- 49 H. Tsunetsugu, T. Ishitobi, and K. Hattori, J. Phys. Soc. Jpn. **90**, 043701 (2021).
- 50 K. Hattori, T. Ishitobi, and H. Tsunetsugu, Phys. Rev. B **107**, 205126 (2023).
- 51 H. T. Ueda, Y. Akagi, and N. Shannon, Phys. Rev. A **93**, 021606(R) (2016).
- 52 R. H. Swendsen and J. S. Wang, Phys. Rev. Lett. **57**, 2607 (1986).
- 53 K. Hukushima and K. Nemoto, J. Phys. Soc. Jpn. **65**, 1604 (1996).
- 54 B. Nienhuis, in *Phase Transitions and Critical Phenomena*, edited by C. Domb and J. L. Lebowitz, Vol. 11 (Academic Press, London, 1987).
- 55 F. Y. Wu, Rev. Mod. Phys. **54**, 235 (1982).
- 56 R. J. Creswick and S.-Y. Kim, J. Phys. A **30**, 8785 (1997).
- 57 R. K. P. Zia and D. J. Wallace, J. Phys. A **8**, 1495 (1975).
- 58 E. Domany, M. Schick, and J. S. Walker, Phys. Rev. Lett. **38**, 1148 (1977).
- 59 P. Bak and J. von Boehm, Phys. Rev. B **21**, 5297 (1980).
- 60 D. R. Nelson and B. I. Halperin, Phys. Rev. B **19**, 2457 (1979).
- 61 S. N. Coppersmith, D. S. Fisher, B. I. Halperin, P. A. Lee, and W. F. Brinkman, Phys. Rev. B **25**, 349 (1982).
- 62 D. F. Agterberg, M. Geracie, and H. Tsunetsugu, Phys. Rev. B **84**, 014513 (2011).
- 63 L. J. P. Ament, M. van Veenendaal, T. P. Devereaux, J. P. Hill, and J. van den Brink, Rev. Mod. Phys. **83**, 705 (2011).
- 64 F. d. Groot, Coord. Chem. Rev. **249**, 31 (2005).
- 65 T. Onimaru, T. Sakakibara, N. Aso, H. Yoshizawa, H. S. Suzuki, and T. Takeuchi, Phys. Rev. Lett. **94**, 197201 (2005).
- 66 M. R. McCarter, K. T. Kim, V. A. Stoica, S. Das, C. Klewe, E. P. Donoway, D. M. Burn, P. Shafer, F. Rodolakis, M. A. P. Gonçalves, F. Gómez-Ortiz, J. Íñiguez, P. García-Fernández, J. Junquera, S. W. Lovesey, G. van der Laan, S. Y. Park, J. W. Freeland, L. W. Martin, D. R. Lee, and R. Ramesh, Phys. Rev. Lett. **129**, 247601 (2022).
- 67 N. Saigal, L. Klebl, H. Lambers, S. Bahmanyar, V. Antić, D. M. Kennes, T. O. Wehling, and U. Wurstbauer, Phys. Rev. Lett. **133**, 046902 (2024).
- 68 N. A. Mikushina and A. S. Moskvin, Phys. Lett. A **302**, 8 (2002).
- 69 Y. Akagi, Y. Amari, N. Sawado, and Y. Shnir, Phys. Rev. D **103**, 065008 (2021).
- 70 Y. Amari, Y. Akagi, S. B. Gudnason, M. Nitta, and Y. Shnir, Phys. Rev. B **106**, L100406 (2022).
- 71 K. Remund, R. Pohle, Y. Akagi, J. Romhányi, and N. Shannon, Phys. Rev. Research **4**, 033106 (2022).
- 72 H. Zhang, Z. Wang, D. Dahlbom, K. Barros, and C. D. Batista, Nat. Commun. **14**, 3626 (2023).
- 73 S. Hayami, Phys. Rev. B **109**, 054422 (2024).
- 74 S. Hayami and K. Hattori, J. Phys. Soc. Jpn. **92**, 124709 (2023).
- 75 K. Hattori and H. Tsunetsugu, J. Phys. Soc. Jpn. **83**, 034709 (2014).
- 76 K. Hattori and H. Tsunetsugu, J. Phys. Soc. Jpn. **85**, 094001 (2016).
- 77 G. Schumm, H. Shao, W. Guo, F. Mila, and A. W. Sandvik, Phys. Rev. B **109**, L140408 (2024).